J. Fluid Mech. (2010), *vol.* 644, *pp.* 395–431.
doi:10.1017/S0022112009992473

Secondary instabilities in the flow around two circular cylinders in tandem

BRUNO S. CARMO[1]†, JULIO R. MENEGHINI[2] AND SPENCER J. SHERWIN[1]

[1]Department of Aeronautics, Imperial College London, South Kensington Campus, London SW7 2AZ, UK

[2]NDF, Department of Mechanical Engineering, Poli, University of São Paulo, SP, Brazil

(Received 30 March 2009; revised 23 September 2009; accepted 24 September 2009)

Direct stability analysis and numerical simulations have been employed to identify and characterize secondary instabilities in the wake of the flow around two identical circular cylinders in tandem arrangements. The centre-to-centre separation was varied from 1.2 to 10 cylinder diameters. Four distinct regimes were identified and salient cases chosen to represent the different scenarios observed, and for each configuration detailed results are presented and compared to those obtained for a flow around an isolated cylinder. It was observed that the early stages of the wake transition changes significantly if the separation is smaller than the drag inversion spacing. The onset of the three-dimensional instabilities were calculated and the unstable modes are fully described. In addition, we assessed the nonlinear character of the bifurcations and physical mechanisms are proposed to explain the instabilities. The dependence of the critical Reynolds number on the centre-to-centre separation is also discussed.

1. Introduction

When two or more bodies are in close proximity and immersed in a fluid stream, the forces experienced by these bodies and the flow field that surrounds them are significantly different from those that are observed when either body is isolated in the same fluid stream. The effect of the presence of other bodies in the flow is called flow interference, and it has crucial importance in aerodynamics and hydrodynamics. One of the most severe types of interference is wake interference, which happens when a body is placed behind another in relation to the free stream. In such situations, the flow impinging on the downstream body is usually completely different from the free stream. The flow around two identical circular cylinders of diameter D in tandem arrangements, separated by a centre-to-centre distance L_x is a very useful model to study wake interference (figure 1). This configuration is simple in geometry, but complex in terms of flow phenomena at low Reynolds numbers, since the flow reaching the downstream cylinder is unsteady and has a dominant frequency; in addition, different vortex shedding regimes are observed depending on the distance between the bodies.

Early scientific works on wake interference in the flow around bluff bodies can be traced back to the first half of the twentieth century. They were mainly concerned with the forces on structural components in tandem arrangements, as, for example,

† Email address for correspondence: bruno.carmo05@imperial.ac.uk

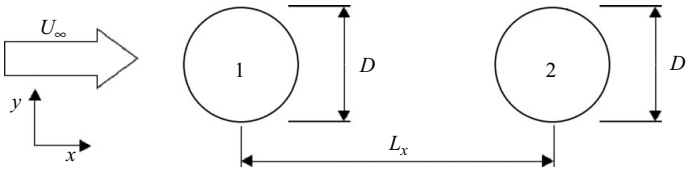

FIGURE 1. Sketch of the flow around two circular cylinders in tandem arrangement.

the work of Biermann & Herrnstein Jr (1933). One of the most important features of the flow around circular cylinders in tandem was identified in these papers: the discontinuity in the value of the aerodynamic forces when the centre-to-centre distance is varied continuously. The separation for which this discontinuity appeared was named *critical spacing* or *critical separation*, and it was soon evident that it depends on the Reynolds number. It is also common to refer to this separation as *drag inversion separation*, since the drag on the downstream cylinder is usually negative in relation to the free-stream direction for separations shorter than the critical and positive for separations larger than the critical (from this point on, the term drag inversion will be used in order to avoid confusion, since the term 'critical' is used to refer to the Reynolds number at the onset of the secondary instabilities). Later, experimental results were published which relied on flow visualization to explain some of the physics associated with wake interference. Thomas & Kraus (1964) tested different centre-to-centre distances under the same Reynolds number ($Re = 62$), and observed that the vortices in the wake behaved differently according to the distance between the cylinders. Zdravkovich (1972) extended this by changing the Reynolds number as well as the centre-to-centre distance. He observed that the transition to turbulence in the wake seemed to occur later in terms of Reynolds number if the spacing was less than the drag inversion separation.

Later publications on the flow around circular cylinders in tandem started to focus on the classification of different flow regimes depending on Reynolds number and centre-to-centre distance. Each flow regime was associated to a wake configuration and aerodynamic force behaviour. Well-regarded examples of this kind of publication are Zdravkovich (1977), Igarashi (1981) and Zdravkovich (1987). Although the classifications differed in the level of detail presented, all agreed on the existence of the above-mentioned discontinuity in the aerodynamic forces, and that this was associated to a very significant change in the vortex configuration in the wake.

The first computational works on tandem arrangements aimed to reproduce these flow regimes by means of numerical simulations. Diverse two-dimensional methods were used, including the discrete vortex method (Slaouti & Stansby 1992) and the finite element method (Mittal, Kumar & Raghuvanshi 1997; Meneghini *et al.* 2001). In general, their research reproduced the regimes qualitatively, and were successful in clearly showing that the drag inversion separation also depended on the Reynolds number due to the change in the formation length with the variation of this parameter, particularly when the flow is two-dimensional. However, they failed to quantitatively match the drag inversion separation with the experimental results for $Re \geqslant 200$, because of the presence of three-dimensional structures in the real flow for such Reynolds numbers.

Recently, more sophisticated studies employed stability theory to approach the problem. Mizushima & Suehiro (2005) investigated the stability and transition of the steady flow around two circular cylinders in tandem by means of numerical simulation and stability analysis. Their results, showed that the presence of the second cylinder

downstream stabilized the flow, and the transition from steady to time-periodic flow occurred at a higher Reynolds number when compared to the transition to time-periodic flow around a single cylinder. They also showed that, for centre-to-centre distances between $3.0D$ and $4.0D$, the origin of the abrupt change in integral quantities, such as the drag coefficient and Strouhal number, was the existence of multiple stable solutions of the flow. The existence of these different stable solutions led to hysteresis and, depending on the centre-to-centre distance, saddle node or subcritical bifurcations were observed. This is significantly different from the isolated cylinder case, in which the primary instability is a Hopf bifurcation (two-dimensional steady to two-dimensional unsteady) of supercritical character. Later, Tasaka *et al.* (2006) reproduced some of the findings of Mizushima & Suehiro (2005) in experiments in a water channel. In 2006, three works using three-dimensional direct numerical simulations of the flow around tandem arrangements were published independently, almost at the same time. Deng *et al.* (2006) employed the virtual boundary method to perform two- and three-dimensional simulations of selected configurations. Their main conclusion was that the transition to three-dimensional flow in the wake was delayed if the cylinders were separated by a distance smaller than the drag inversion spacing. Carmo & Meneghini (2006) performed two- and three-dimensional simulations for diverse centre-to-centre distances at Reynolds numbers in the range of early wake transition ($160 < Re < 320$). Using Strouhal number data and vorticity contours, it was concluded that the presence of three-dimensional structures affected the flow in different ways, depending on the interference regime. For small centre-to-centre distance ($L_x/D = 1.5$), no significant differences were observed in the forces on the bodies when comparing the two- and three-dimensional results. For L_x close to the drag inversion separation, the two- and three-dimensional results were completely different: for two-dimensional simulations the drag inversion occurred for $3.0 \leqslant L_x/D \leqslant 3.5$ in the Reynolds number range investigated, whereas for the three-dimensional results the drag on the downstream cylinder was always negative for these L_x. Finally, for configurations in which the vortices detached from the upstream cylinder before impinging on the downstream cylinder, the three-dimensional structures had the same effects on the forces on the pairs of cylinders as they did on a single cylinder, suggesting that the early wake transition route was the same for these arrangements as for the single cylinder. In order to identify the effects of three-dimensional structures and cylinder spacing, Papaioannou *et al.* (2006) also performed two- and three-dimensional simulations of the flow around two circular cylinders in tandem. They observed that two-dimensional simulations under-predicted the drag inversion spacing. In addition, they noticed that, for three-dimensional fluctuations, the presence of the downstream cylinder at centre-to-centre distances less than the drag inversion spacing had a stabilizing effect, whereas if the downstream cylinder was placed at a distance greater than the drag inversion spacing, it had a destabilizing effect.

Although these investigations have indicated that the presence of three-dimensional structures greatly affects the observed flow regime and that, depending on the centre-to-centre distance, the three-dimensional structures in the wake can be considerably different from those observed in the flow around a single cylinder, no paper has yet fully characterized the modes, mechanisms and onsets of the three-dimensional instabilities in the time-periodic wake of the flow around circular cylinders in tandem arrangements. The goal of the present work is to use asymptotic stability theory and direct numerical simulation to study the early stages of the wake transition for different geometrical configurations, which were chosen according to the two-dimensional flow regime observed.

This paper is organized as follows. First, in § 2, we present the numerical tools used in the present work. In § 3 a summary of previously published results regarding the flow around an isolated cylinder is given as a benchmark for the new data on the flow around tandem arrangements. Details of the calculations performed are given in § 4 and the results are presented and analysed in § 5. Further discussion on the relationship between centre-to-centre separation, secondary instabilities and respective physical mechanisms is presented in § 6. Finally, in § 7, the main findings are summarized and conclusions regarding their implications are drawn.

2. Numerical method

2.1. *Linear stability analysis*

The method employed for the linear stability calculations in this paper consisted in testing the stability of two-dimensional time-periodic flows, which are called base flows, to three-dimensional infinitesimal perturbations, using Floquet theory. The base flows were obtained by means of two-dimensional numerical simulations of the incompressible Navier–Stokes equations, here written in non-dimensional form:

$$\frac{\partial \boldsymbol{u}}{\partial t} = -(\boldsymbol{u}\cdot\nabla)\boldsymbol{u} - \nabla p + \frac{1}{Re}\nabla^2\boldsymbol{u}, \tag{2.1}$$

$$\nabla\cdot\boldsymbol{u} = 0. \tag{2.2}$$

The cylinder diameter D is the reference length and the free-stream speed U_∞ is the reference speed used in the non-dimensionalization. $\boldsymbol{u}\equiv(u, v)$ is the velocity field, t is the time, p is the static pressure, $Re = \rho U_\infty D/\mu$ is the Reynolds number and μ is the dynamic viscosity of the fluid. The pressure was assumed to be scaled by the constant density ρ. The numerical solution of these equations was calculated using a spectral/hp discretization as presented in Karniadakis & Sherwin (2005). The time integration scheme adopted was the stiffly stable splitting scheme presented by Karniadakis, Israeli & Orszag (1991).

For the stability calculations, a bi-global direct stability analysis methodology similar to that utilized in Barkley & Henderson (1996) was employed. The two-dimensional T-periodic base flows $\boldsymbol{U}(x, y, t)$ were tested against an infinitesimal three-dimensional perturbation $\boldsymbol{u}'(x, y, z, t)$, whose evolution was governed by the linearized three-dimensional Navier–Stokes equations:

$$\frac{\partial \boldsymbol{u}'}{\partial t} = -(\boldsymbol{U}\cdot\nabla)\boldsymbol{u}' - (\boldsymbol{u}'\cdot\nabla)\boldsymbol{U} - \nabla p' + \frac{1}{Re}\nabla^2\boldsymbol{u}', \tag{2.3}$$

$$\nabla\cdot\boldsymbol{u}' = 0, \tag{2.4}$$

where $p'(x, y, z, t)$ is the pressure perturbation. Homogeneous boundary conditions $\boldsymbol{u}' = 0$ were imposed on the boundaries where the base flow had Dirichlet boundary conditions, and $\partial\boldsymbol{u}'/\partial\boldsymbol{n} = 0$ was imposed on the boundaries where Neumann conditions were specifed for the base flow.

Since (2.3) and (2.4) are linear and time periodic (because of their dependence on the time-periodic field $\boldsymbol{U}$), the stability of this system can be investigated using Floquet theory. The solution of (2.3) subjected to (2.4) is a sum of functions of the form $\tilde{\boldsymbol{u}}(x, y, z, t)\mathrm{e}^{\sigma t}$, where $\tilde{\boldsymbol{u}}(x, y, z, t)$, which are called Floquet modes, are T-periodic solutions. These solutions are obtained by employing an Arnoldi algorithm, in the way explained in Carmo *et al.* (2008) and based on the earlier work of Tuckerman & Barkley (2000). The action of the linearized Navier–Stokes equations (2.3)–(2.4) on

the perturbation $\boldsymbol{u}'$ is needed for this algorithm, and this action is calculated by numerically integrating the equations in a way similar to that employed to integrate the base flow. The only differences are in the calculation of the nonlinear term, and in the calculation of the derivatives in the z direction (see Barkley & Henderson 1996, for details). The stability of the system is given by the sign of the real parts of the Floquet exponents σ. In Floquet analysis, however, it is more common to use the Floquet multiplier $\mu \equiv \mathrm{e}^{\sigma T}$ when displaying the results. The stability criterion is, thus, that the system is stable if $|\mu| < 1$, unstable if $|\mu| > 1$ and neutrally stable if $|\mu| = 1$.

Still, following Barkley & Henderson (1996), the system can be further simplified, since the spanwise direction z is homogeneous. In such cases, the velocity perturbation field can be written as a Fourier integral:

$$\boldsymbol{u}'(x, y, z, t) = \int_{-\infty}^{\infty} \hat{\boldsymbol{u}}(x, y, \beta, t)\mathrm{e}^{\mathrm{i}\beta z}\,\mathrm{d}\beta \tag{2.5}$$

and similarly for p'. Since we are dealing with the linearized Navier–Stokes equations, modes with different β do not couple, and the velocity components $(\hat{u}, \hat{v}, \hat{w})$ and pressure $\hat{p}$ depend only on x, y and t. Therefore, given a geometrical configuration, the three-dimensional stability analysis for each Reynolds number can be carried out by performing a series of two-dimensional stability calculations with different wavenumbers β. Further details on the algorithms for the stability calculations are given in Carmo *et al.* (2008).

For the analysis of the stability results, it is useful to write the linearized Navier–Stokes equations using the vorticity–velocity formulation. Taking the curl of (2.3) and (2.4), we get

$$\frac{\partial \boldsymbol{\omega}'}{\partial t} = -(\boldsymbol{U}\cdot\nabla)\boldsymbol{\omega}' - (\boldsymbol{u}'\cdot\nabla)\boldsymbol{\Omega} + (\boldsymbol{\Omega}\cdot\nabla)\boldsymbol{u}' + (\boldsymbol{\omega}'\cdot\nabla)\boldsymbol{U} + \frac{1}{Re}\nabla^2\boldsymbol{\omega}', \tag{2.6}$$

$$\nabla\cdot\boldsymbol{\omega}' = 0, \tag{2.7}$$

where $\boldsymbol{\omega}'$ and $\boldsymbol{\Omega}$ are the perturbation and base flow vorticity vectors, respectively. Since the base flow is two-dimensional, i.e. $\boldsymbol{U} = (U(x, y, t), V(x, y, t), 0)$ and $\boldsymbol{\Omega} = (0, 0, \Omega_z(x, y, t))$, we can write (2.6) for the three components of the perturbation vorticity $(\boldsymbol{\omega}' = (\omega_x', \omega_y', \omega_z'))$ as

$$\frac{\partial \omega_x'}{\partial t} + U\frac{\partial \omega_x'}{\partial x} + V\frac{\partial \omega_x'}{\partial y} = \omega_y'\frac{\partial U}{\partial y} + \Omega_z\frac{\partial u'}{\partial z} + \omega_x'\frac{\partial U}{\partial x} + \frac{1}{Re}\nabla^2\omega_x', \tag{2.8}$$

$$\frac{\partial \omega_y'}{\partial t} + U\frac{\partial \omega_y'}{\partial x} + V\frac{\partial \omega_y'}{\partial y} = \omega_x'\frac{\partial V}{\partial x} + \Omega_z\frac{\partial v'}{\partial z} + \omega_y'\frac{\partial V}{\partial y} + \frac{1}{Re}\nabla^2\omega_y', \tag{2.9}$$

$$\frac{\partial \omega_z'}{\partial t} + U\frac{\partial \omega_z'}{\partial x} + V\frac{\partial \omega_z'}{\partial y} + u'\frac{\partial \Omega_z}{\partial x} + v'\frac{\partial \Omega_z}{\partial y} = \Omega_z\frac{\partial w'}{\partial z} + \frac{1}{Re}\nabla^2\omega_z'. \tag{2.10}$$

The first terms on the left-hand side of these equations are the local time derivatives of perturbation vorticity. The remaining terms on the left-hand side account for the advection of vorticity. The first two terms on the right-hand side of (2.8) and (2.9) correspond to vortex tilting, and the third term in (2.8) and (2.9) and first term in (2.10) are vortex stretching terms. Finally, the last term in all three equations denotes perturbation vorticity diffusion.

2.2. *Nonlinear analysis*

The linearized Navier–Stokes equations are valid provided that the perturbation is very small compared to the base flow. If the perturbation is unstable as predicted by the linear stability analysis, it will grow exponentially and will eventually reach an amplitude for which nonlinear interactions must be taken into account. In order to study the effects of these interactions on the growth of the perturbation and to characterize the final state of the complete nonlinear system after the bifurcation, nonlinear simulations were employed.

These simulations were performed using a three-dimensional version of the Navier–Stokes solver which uses Jacobi polynomials in the spatial discretization in the xy plane and Fourier modes in the spanwise direction (Karniadakis 1990). The spanwise dimension of the domain was equal to the wavelength of the perturbation and periodic boundary conditions were used on the top and bottom of the domain. The Reynolds number chosen was slightly higher than that of the bifurcation given by the linear stability analysis. The initial condition was the base flow summed to the unstable perturbation with very low energy. The flow was allowed to evolve so the initial linear growth of the perturbation could be observed, followed by the manifestation of nonlinear interactions and finally the saturation of the growth at a new fully developed state.

The evolution of hydrodynamic systems at Reynolds numbers close to a bifurcation was often successfully modelled by the Landau equation (Provansal, Mathis & Boyer 1987; Henderson 1997; Sheard, Thompson & Hourigan 2004). This equation describes the evolution of the amplitude $A(t)$ of the perturbation and can be written as

$$\frac{\mathrm{d}A}{\mathrm{d}t} = (\alpha + \imath\omega)\, A - l\,(1 + \imath c)\,|A|^2 A + \cdots, \tag{2.11}$$

truncating the equation at the third-order term. The parameter α is the linear growth rate of the perturbation, which corresponds to the real part of the exponent obtained from the linear stability analysis. The term ω is the angular oscillation frequency of the perturbation energy during the linear growth phase. For bifurcations with synchronous modes (imaginary part of the Floquet exponent equals to zero), ω is equal to the oscillation frequency of the base flow. The growth of the linear part is eventually counter-balanced by the terms of higher order, since the physical system is bounded. The role of the third-order term is of special interest, since it determines if the bifurcation is supercritical or subcritical. The sign of the coefficient l in (2.11) indicates the type of the bifurcation: if $l > 0$ the bifurcation is supercritical and if $l < 0$ the bifurcation is subcritical. Supercritical bifurcations are non-hysteretic and can usually be fully described by the Landau equation truncated at third order. On the other hand, subcritical bifurcations generally present hysteresis and terms of order higher than the third in the Landau equation are needed to adequately describe the behaviour of the system, since both the linear- and third-order terms contribute to the growth of the system. Finally, c is the Landau constant and its effect is to modify the oscillation frequency of the system.

To obtain the values of l and c, we write the complex amplitude A in polar form, $A(t) = \rho(t)\mathrm{e}^{\imath\Phi(t)}$. The real variable $\rho = |A|$ describes the mode amplitude, and the real variable Φ describes the phase of the mode. The real and imaginary parts of (2.11)

then read as

$$\frac{\mathrm{d}\log(\rho)}{\mathrm{d}t} = \alpha - l\rho^2, \tag{2.12}$$

$$\frac{\mathrm{d}\boldsymbol{\Phi}}{\mathrm{d}t} = \omega - lc\rho^2. \tag{2.13}$$

If we plot the value of $\mathrm{d}\log(|A|)/\mathrm{d}t$ against $|A|^2$, (2.12) can be used to determine the values of α and l: α is the value of $\mathrm{d}\log(|A|)/\mathrm{d}t$ when $|A|^2 = 0$ and l is equal to minus the value of the slope of the curve. If the graph is linear at large $|A|^2$ it means that the Landau equation truncated at third order is sufficient to describe the evolution of the system. The value of the Landau constant c can be obtained considering that at saturation A oscillates with frequency ω_{sat}, so

$$\frac{\mathrm{d}\boldsymbol{\Phi}}{\mathrm{d}t} = \omega_{sat} = \omega - lc\rho_{sat}^2.$$

From (2.12), we obtain $\rho_{sat}^2 = \alpha/l$. Therefore, we can write

$$c = \frac{\omega - \omega_{sat}}{\alpha}.$$

A final note should be given on the definition of the amplitude A. In this work, the same definition used in Carmo *et al.* (2008) is adopted:

$$|A(t)| = \left[\int_{\Omega} |\hat{\boldsymbol{u}}_{\mathbf{1}}(x, y, t)|^2\right]^{1/2}.$$

Ω is the two-dimensional cross-section of the domain being considered and $\hat{\boldsymbol{u}}_{\mathbf{1}}(x, y, t)$ is the coefficient of the Fourier mode corresponding to the perturbation being investigated.

3. Secondary instabilities in the wake for the flow around a single cylinder

In this section, a summary about the secondary instabilities observed in the wake of the flow around a single cylinder is presented in order to provide a benchmark to which the results presented in the next section will be compared. The reader interested in more details about these results should refer to Barkley & Henderson (1996) and Blackburn, Marques & Lopez (2005) for the linear stability analysis results and to Henderson (1997) for the nonlinear analysis. The main results presented in these references were reproduced in Carmo *et al.* (2008) using the same code that was used in the present work. A very comprehensive account on the secondary instabilities from the experimental point of view is given in Williamson (1996).

In figure 2(*a*) the modulus of the Floquet multiplier $|\mu|$ is plotted as a function of the non-dimensional spanwise wavenumber βD for various Reynolds numbers. The values of $|\mu|$ increase with Re and unstable values ($|\mu| > 1$) are observed at two distinct peaks in the curves. Using the nomenclature introduced by Williamson (1988), the peak for lower βD corresponds to mode A and that for higher βD corresponds to mode B. The Floquet multiplier for both modes is purely real and positive. The neutral stability curves are shown in figure 2(*b*). It can be seen that mode A becomes unstable earlier, at $Re_A = 190 \pm 1$ with a wavelength $\lambda_{zA}/D = 3.97 \pm 0.01$ ($\beta_A D = 1.58$), and mode B becomes unstable at $Re_B = 260.5 \pm 1.0$ with a wavelength $\lambda_{zB}/D = 0.825 \pm 0.010$ ($\beta_B D = 7.62$). In the present work, we will be more concerned with these two modes that first become unstable as the Reynolds number is increased;

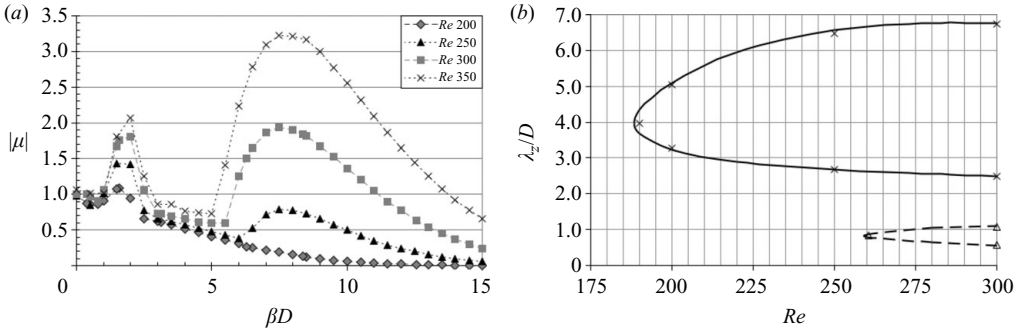

FIGURE 2. Flow around a single cylinder. (*a*) Modulus of the Floquet multiplier $|\mu|$ as a function of the spanwise wavenumber times the cylinder diameter βD for various Reynolds numbers. (*b*) Neutral stability curves (curves that pass through points where $|\mu| = 1$), plotted in a map of Reynolds number (x-axis) and mode non-dimensional wavelength (y-axis); in the region on the right-hand side of the curves the two-dimensional periodic flow is unstable with respect to three-dimensional perturbations; continuous and dashed curves are from Barkley & Henderson (1996) and refer to modes A and B, respectively; $\times$ represent mode A neutral points and $\triangle$ represent mode B neutral points from Carmo *et al.* (2008).

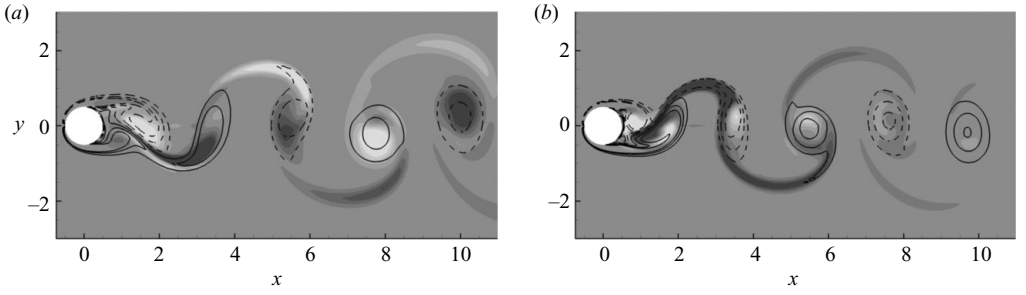

FIGURE 3. Floquet mode x vorticity contours and base flow z vorticity iso-lines, single cylinder. Light contours and dashed lines are negative vorticity and dark contours and solid lines are positive vorticity. (*a*) Mode A: $Re = 200$, $\beta D = 1.571$; (*b*) mode B: $Re = 300$, $\beta D = 7.570$.

however, it is worth noting that, besides modes A and B, the wake of the flow around a single cylinder also becomes unstable to a quasi-periodic mode (the Floquet multiplier is complex) at $Re_{QP} \approx 377$ with $\lambda_{zQP}/D \approx 1.8$ $\left(\beta_{QP} D \approx 3.49\right)$ (Blackburn *et al.* 2005).

In addition to the critical Reynolds numbers and wavelengths, modes A and B also show differences regarding their spatio-temporal symmetries. It is usual to visualize the structure of these three-dimensional modes using streamwise vorticity contours ($\tilde{\omega}_x$). The symmetry observed for mode A using such contours is

$$\tilde{\omega}_x(x, y, z, t) = -\tilde{\omega}_x(x, -y, z, t + T/2), \tag{3.1}$$

while for mode B it reads

$$\tilde{\omega}_x(x, y, z, t) = \tilde{\omega}_x(x, -y, z, t + T/2). \tag{3.2}$$

These symmetries are shown in a graphic way in figure 3. For mode A, the Floquet mode x vorticity has different sign either side of the wake centreline, whereas for mode B the mode x vorticity has the same sign throughout the cycle. In the same figure, it can be seen that mode A has stronger streamwise vorticity contours in the

base flow vortex cores, while for mode B the stronger three-dimensional structures are observed in the shear layers that link the cores.

Regarding the nonlinear character of the bifurcations, Henderson (1997) showed that mode A bifurcates through a subcritical route that causes a reduction in the primary oscillation frequency of the wake at saturation. On the other hand, mode B bifurcates through a supercritical route with no frequency shift near the threshold.

4. Computational simulations

The study of the secondary instabilities in the flow around two circular cylinders in tandem arrangements is more complicated than in the case of an isolated cylinder since there are two control parameters, namely the Reynolds number and cylinder separation. In § 5, detailed results are presented for four different configurations, which are tandem arrangements with centre-to-centre distances of $1.5D$, $1.8D$, $2.3D$ and $5.0D$. These configurations were chosen after a number of calculations were performed, and they are representative of the four different scenarios encountered for $L_x/D \geqslant 1.2$. Care was taken to ensure that these specific cases capture all possible scenarios observed, with accuracy of $0.1D$ in the separation.

The base flow for the configurations with $L_x/D = 1.5$, $L_x/D = 1.8$, $L_x/D = 2.3$ and $L_x/D = 5.0$ in the secondary instability Reynolds number range can be classified in three different shedding regimes, shown in figure 4. For $L_x/D = 1.5$, a pair of almost symmetric vortices are formed in the interstitial region, and the shear layers that separate from the upstream cylinder and reattach to the downstream cylinder are nearly steady upstream from the formation region (the region where the shear layers roll up and form the vortices). We will call this vortex shedding regime *SG* (symmetric in the gap). The graphs in figure 5(*a*, *d*) show that, for configurations at this shedding regime, the root mean square (RMS) of the lift coefficient is very small for both cylinders, and the drag coefficient of the downstream cylinder is negative. For $L_x/D = 1.8$ and $L_x/D = 2.3$, the vortices are not shed in the interstitial region, but there are regions of concentrated vorticity whose sizes grow and decrease alternatively in time. The shear layers that separate from the upstream cylinder and reattach on the downstream cylinder surface flap up and down according to the vortex shedding frequency. We will refer to this regime as *AG* (alternating in the gap). It can be seen in figure 5(*b*, *e*) that the forces on the upstream cylinder do not differ much from what is observed in the shedding regime *SG*, although a decrease in the frequency can be observed. The downstream cylinder, however, experiences a considerable increase in the RMS of the lift coefficient when compared to regime *SG*. Lastly, for $L_x/D = 5$ the vortices are shed in the gap region, and this regime will be referred as *WG* (wake in the gap). Figure 5(*c*, *f*) shows that the RMS of all forces increase greatly and that the drag on the downstream cylinder becomes positive. The discontinuity in the aerodynamic forces mentioned in the introduction happens when the shedding regime changes from *AG* to *WG*. It is interesting to notice that even for regime *WG* the near wakes of the upstream and downstream cylinders are fundamentally different. The near wake of the upstream cylinder exhibits a vortex formation mechanism like that observed for an isolated cylinder, described by Gerrard (1966), whereas the shedding in the near wake of the downstream cylinder appears to be controlled by the upstream wake impinging on the body and no 'true' formation region is observed, as discussed in Carmo *et al.* (2008). We observed hysteresis in both regime transitions: between regimes *SG* and *AG* and between regimes *AG* and *WG*. In a sense, the shedding regimes *SG*, *AG* and *WG* correspond, respectively, to regimes

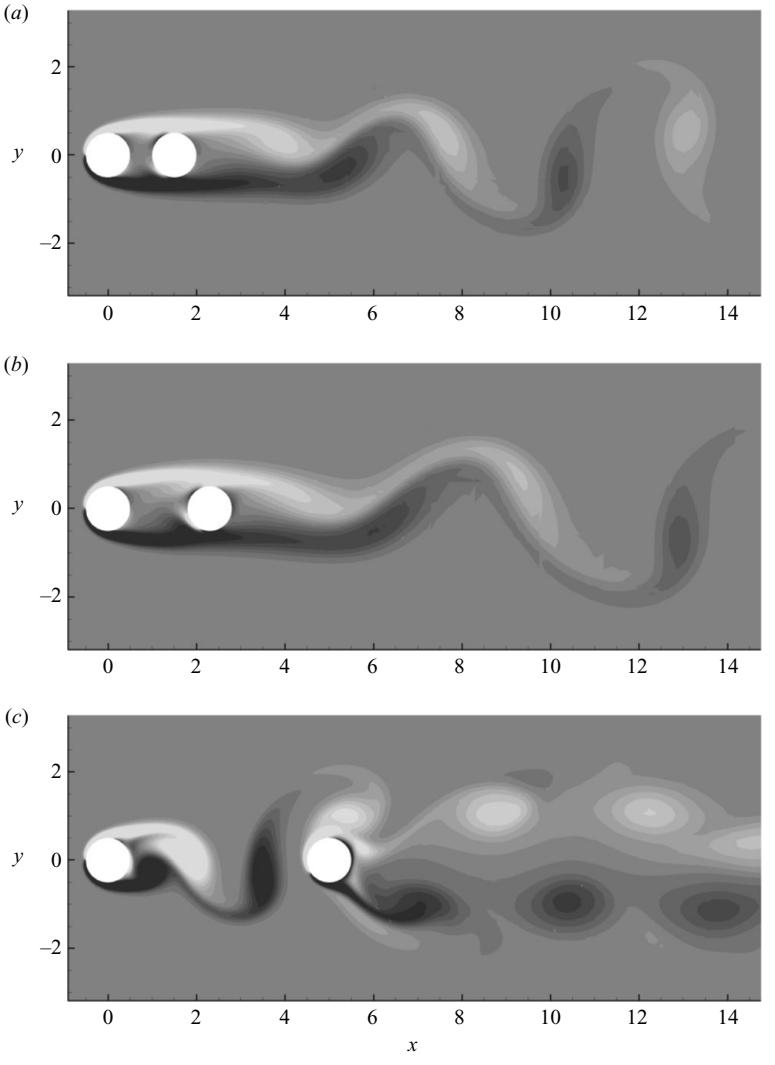

FIGURE 4. Instantaneous vorticity contours, $Re = 200$, two-dimensional simulations. Contours vary from $\omega_z D/U_\infty = -2.2$ (light contours) to $\omega_z D/U_\infty = 2.2$ (dark countours). (*a*) $L_x/D = 1.5$ – regime *SG*; (*b*) $L_x/D = 2.3$ – regime *AG*; (*c*) $L_x/D = 5$ – regime *WG*.

W-*T*1, *W*-*T*2 and *W*-*T*(1+2) of the classification proposed by Zdravkovich (1987). A significant difference is that Zdravkovich mentioned that in regime *W*-*T*1 the shear layer separating from the upstream cylinder did not reattach on the downstream cylinder, while this reattachment was observed to occur for all configurations studied in the current work.

The results are presented for Reynolds numbers in the transition range for each of the cases and the non-dimensional perturbation spanwise wavenumbers investigated varied from 0.0 to 15.0. The base flow was generated by means of two-dimensional simulations using a mesh whose upstream boundary was located 36*D* from the centre of the upstream cylinder, the downstream boundary located 45*D* from the centre of the downstream cylinder and the side boundaries located at 50*D* from the centre of the bodies, as can be seen in figure 6(*a*). The number of elements varied from

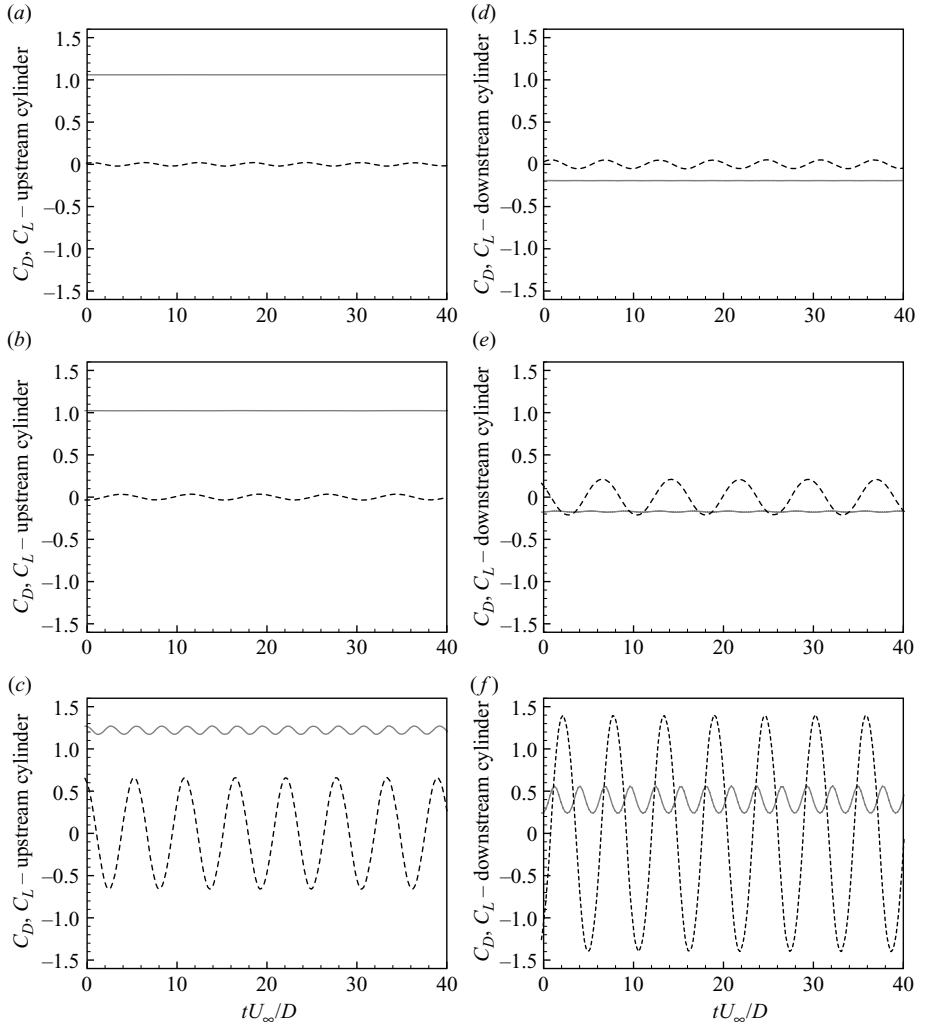

FIGURE 5. Drag coefficient (grey solid line) and lift coefficient (black dashed line) time series for the upstream and downstream cylinders, $Re = 200$, two-dimensional simulations. The scale of the graphs is the same for ease of comparison. (a, d) $L_x/D = 1.5$ – regime SG; (b, e) $L_x/D = 2.3$ – regime AG; (c, f) $L_x/D = 5$ – regime WG.

554 to 765, depending on the configuration, and polynomials of degree 8 were used as base and test functions. These dimensions and level of discretization were based in a previous convergence study carried out in Carmo *et al.* (2008). Subsequently, a number of equally spaced in time snapshots were taken over a cycle. We performed a convergence study and concluded that 32 snapshots were sufficient to properly represent the base flow (calculations using 64 snapshots showed variations of less than 0.1 % in the eigenvalue). In order to save computational cost, these snapshots were interpolated into smaller meshes, in which the stability calculations were carried out, using a Krylov subspace of size 10. These meshes had upstream boundary located $8D$ from the upstream cylinder, downstream boundaries located around $24D$ from the downstream cylinder and side boundaries $5D$ far from the centre of the bodies. A typical example of this mesh is depicted in figure 6(e). A convergence analysis was

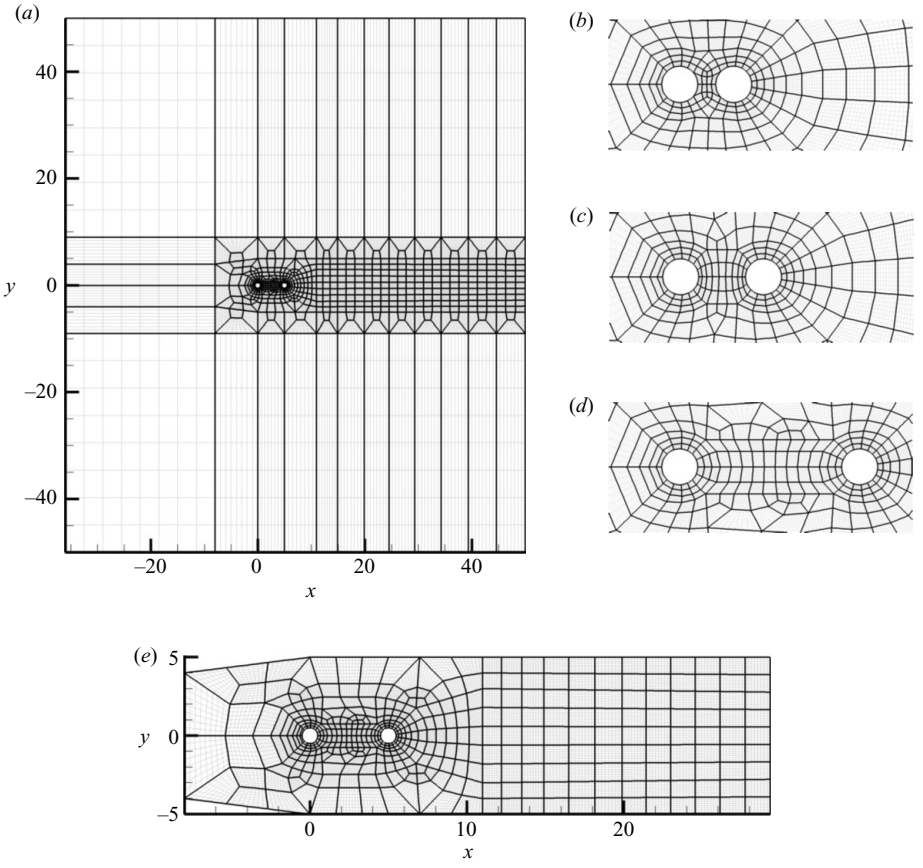

FIGURE 6. Example of mesh used to generate the base flows (*a*), details of the meshes in the vicinity of the cylinders for $L_x/D = 1.5$ (*b*), $L_x/D = 2.3$ (*c*), $L_x/D = 5$ (*d*) and example of mesh used in the stability calculations (*e*).

undertaken to see how the stability results were affected by the dimensions of the mesh. It was verified that the differences between the results obtained with the original mesh and those obtained with the smaller meshes were negligible (less than 0.001 %), as long as the base flow was generated in the original large mesh. This result is in agreement with the convergence studies published in Barkley & Henderson (1996). The nonlinear simulations were performed using the large mesh and 4 Fourier modes were used in the discretization in the spanwise direction.

Bearing in mind that the study carried out by Mizushima & Suehiro (2005) to investigate the primary instability was two-dimensional, a question that can naturally arise is whether the primary instability is indeed from two-dimensional steady flow to two-dimensional time-periodic flow, or if there is a bifurcation to a three-dimensional state (steady or unsteady) prior to that. To answer this question, we have run preliminary calculations to check for three-dimensional instabilities of steady flows at Reynolds numbers slightly below the primary instability as calculated by Mizushima & Suehiro (2005). The configurations tested were $L_x/D = 1.5$, 1.8, 2.3 and 5.0, the Reynolds numbers were 40 for $L_x/D = 5.0$ and 70 for the other three configurations, and the non-dimensional spanwise wavenumbers varied from 0.0 to 15.0. The flows were stable for all cases with no discernible peak approaching the stability threshold.

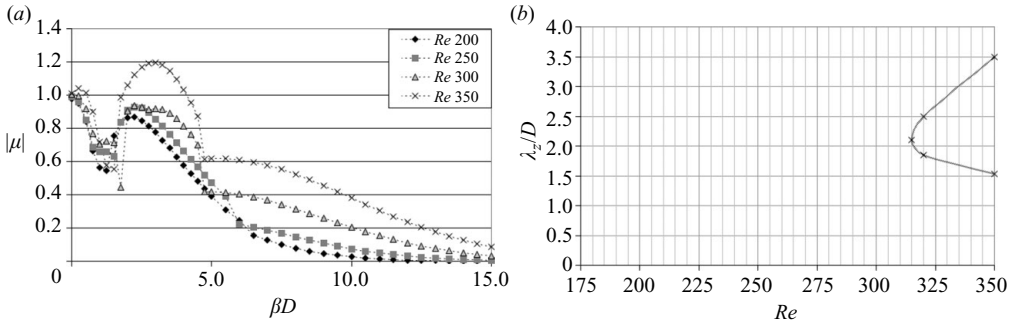

FIGURE 7. Flow around two circular cylinders in tandem with $L_x/D = 1.5$. (*a*) Modulus of Floquet multiplier as a function of the non-dimensional spanwise wavenumber, (*b*) neutral stability curves.

Therefore, we concluded that the primary instability is indeed from two-dimensional steady flow to two-dimensional unsteady flow for the type of arrangement investigated in this paper.

5. Results – flow around circular cylinders in tandem arrangements

In the following subsections, each of the different scenarios for the secondary instability that were observed are analysed in detail. Results from the linear stability calculations and nonlinear simulations of representative configurations are presented, and physical mechanisms to explain the instabilities are proposed.

5.1. *Configuration* $L_x/D = 1.5$ – *shedding regime SG*

For all cases in which the shedding regime was of type *SG* (see figure 4*a*), the same secondary instability scenario was observed, and is illustrated by configuration $L_x/D = 1.5$.

5.1.1. *Linear analysis*

Figure 7(*a*) shows the variation of the modulus of the Floquet multiplier according to the perturbation wavenumber for different Reynolds numbers. The figure shows that for $Re \leqslant 300$ the two-dimensional flow is linearly stable to infinitesimal three-dimensional perturbations (the Floquet multipliers have a modulus of less than 1 for all wavenumbers). When the Reynolds number was increased to 350, the flow became unstable to perturbations with a non-dimensional wavenumber $\beta D \approx 3.0$. For the entire Reynolds number range investigated, the least stable mode had a purely real eigenvalue for $\beta D < 5$. The least stable modes for $\beta D \geqslant 5$ all have complex Floquet multipliers.

Further simulations were performed in order to draw the neutral stability curve displayed in figure 7(*b*). The mode that became unstable had its bifurcation point at $Re = 315 \pm 1$, and the unstable eigenmode had a wavenumber of $\beta D = 2.998 \pm 0.002$, corresponding to a wavelength of $\lambda_z/D = 2.096 \pm 0.002$. For ease of reference, we will call this mode T1. The critical Reynolds number for this configuration is much higher than that for the flow around a single cylinder, and the wavelength of the perturbation of maximum growth has a value between the wavelengths of mode A and mode B observed in the isolated cylinder case.

Figure 8 shows the structure of mode T1. It can be seen that mode T1 has a symmetry similar to that of mode B, with the same sign of streamwise vorticity on

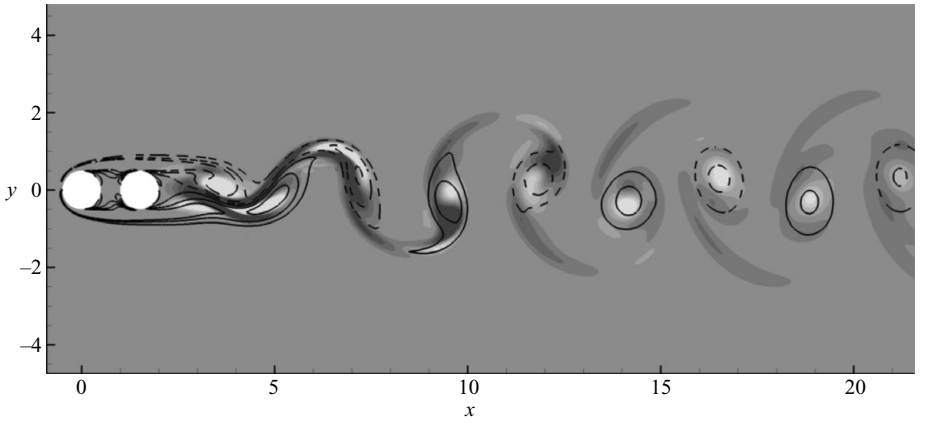

FIGURE 8. Mode T1 x vorticity contours and base flow z vorticity iso-lines, $L_x/D = 1.5$, $Re = 320$, $\beta D = 3.0$. Light contours and dashed lines represent negative vorticity and dark contours and solid lines represent positive vorticity.

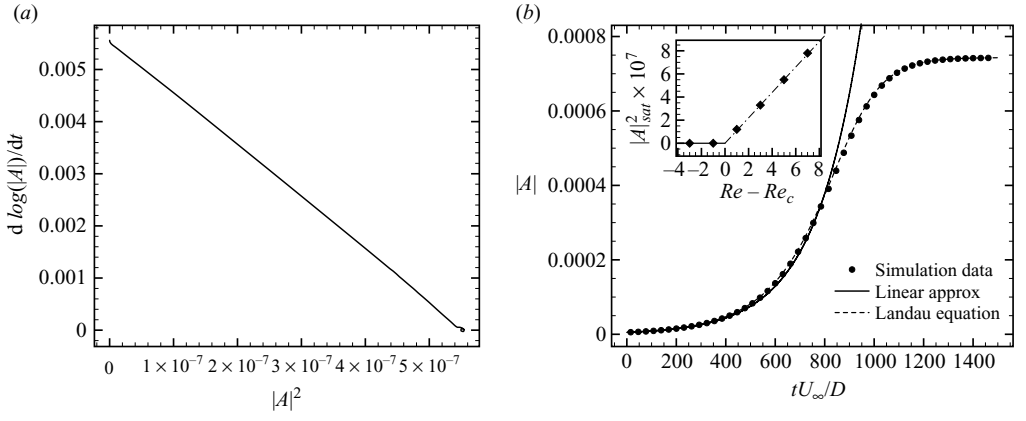

FIGURE 9. Results for three-dimensional nonlinear simulation of case $L_x/D = 1.5$, $Re = 320$, $\beta D = 3.0$ ($L_z/D = 2.094$) – mode T1. (*a*) The graph of the time derivative of the amplitude logarithm against the square of the amplitude. (*b*) The growth and saturation of the perturbation amplitude (symbols), growth predicted by linear calculations (continuous line) and growth predicted by the Landau equation (dashed line). The inset shows the bifurcation diagram in which the supercritical character is also clear.

both sides of the wake. Another similarity is that both modes (T1 and B) have strong streamwise vorticity in the shear layers that link the cores, although mode T1 also shows significant x vorticity values in the vortex cores. Also worth noting is the fact that mode T1 and the single cylinder mode B have completely different wavenumbers: the non-dimensional wavenumber for mode B is approximately 7.5.

5.1.2. *Nonlinear analysis*

A three-dimensional simulation was carried out in order to assess the nonlinear character of the bifurcation of mode T1 in the flow around the configuration with $L_x/D = 1.5$. The methodology adopted was explained in § 2.2. Figure 9 shows the results of this simulation. The bifurcation is clearly supercritical, and the Landau equation truncated at third-order fits remarkably well to the data. The inset in

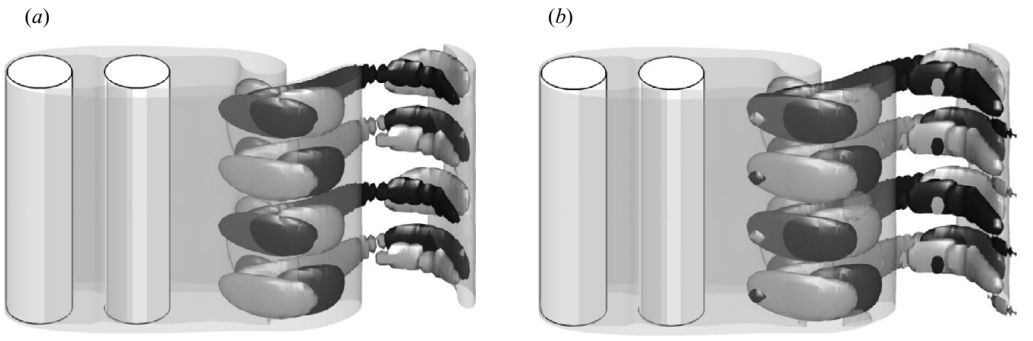

FIGURE 10. Three-dimensional views of the nonlinear results at the saturated state (a) and base flow combined with the unstable Floquet mode (b), $L_x/D = 1.5$, $Re = 320$, $\beta D = 3.0$ – mode T1. Translucent surfaces represent iso-surfaces of $|\omega_z|$. Solid light grey and dark grey surfaces represent iso-surfaces of negative and positive ω_x, respectively.

figure 9(b) shows the bifurcation diagram for this configuration, in which it can be seen that the amplitude squared of the perturbation energy follows a straight line for Reynolds numbers greater than the critical, in the vicinity of the bifurcation. This is also a characteristic of supercritical bifurcations.

Figure 10(a) shows iso-surfaces of vorticity for the saturated state and figure 10(b) shows these iso-surfaces for a linear combination of the base flow and Floquet mode. These figures display the flow fields at roughly the same phase of the shedding cycle. It can be seen that the contours are similar; the three-dimensional structures of the unstable mode remain clearly observable after the nonlinear growth of the perturbation.

5.1.3. *Physical mechanism*

Mode T1 has a number of characteristics that suggest that the physical mechanism responsible for this instability is of hyperbolic type. The basic theory and mathematical formulation of hyperbolic instabilities for viscous fluids were presented by Lagnado, Phan-Thien & Leal (1984), who showed that perturbation streamwise vorticity in a straining base flow field grows due to vortex stretching, and this growth competes with the viscous diffusion. The resulting field exhibits streamwise vorticity aligned with the outlet streamlines of the straining field. This kind of instability has been found in some other flows, like plane shear layers (Lasheras & Choi 1988), and was suggested to be the physical mechanism of mode B in the single cylinder flow (Williamson 1996).

In order to illustrate the physical mechanism of mode T1, figure 11 presents instantaneous base flow streamtraces superposed to Floquet mode x vorticity contours. Using the arbitrary time scale indicated in the figure, it can be seen that for $T/8$ the base flow has a hyperbolic region close to the recently shed vortex, as indicated by the straining instantaneous streamlines. The perturbation negative streamwise vorticity on the bottom of the figure is amplified through a stretching mechanism (term $\omega_x' \partial U/\partial x$ in (2.8)). Part of this amplified streamwise vorticity is convected upstream and to the opposite side of the wake by the base flow, as shown by the streamtraces pointing left-upwards at instants $T/4$ and $T/8$. By the time a new positive base flow spanwise vortex is formed, the region of streamwise vorticity has already reached the top side of the wake. When the new vortex is shed (instant $T/2$), it provides a new region of hyperbolic flow, which amplifies the streamwise vorticity that is now on the top side

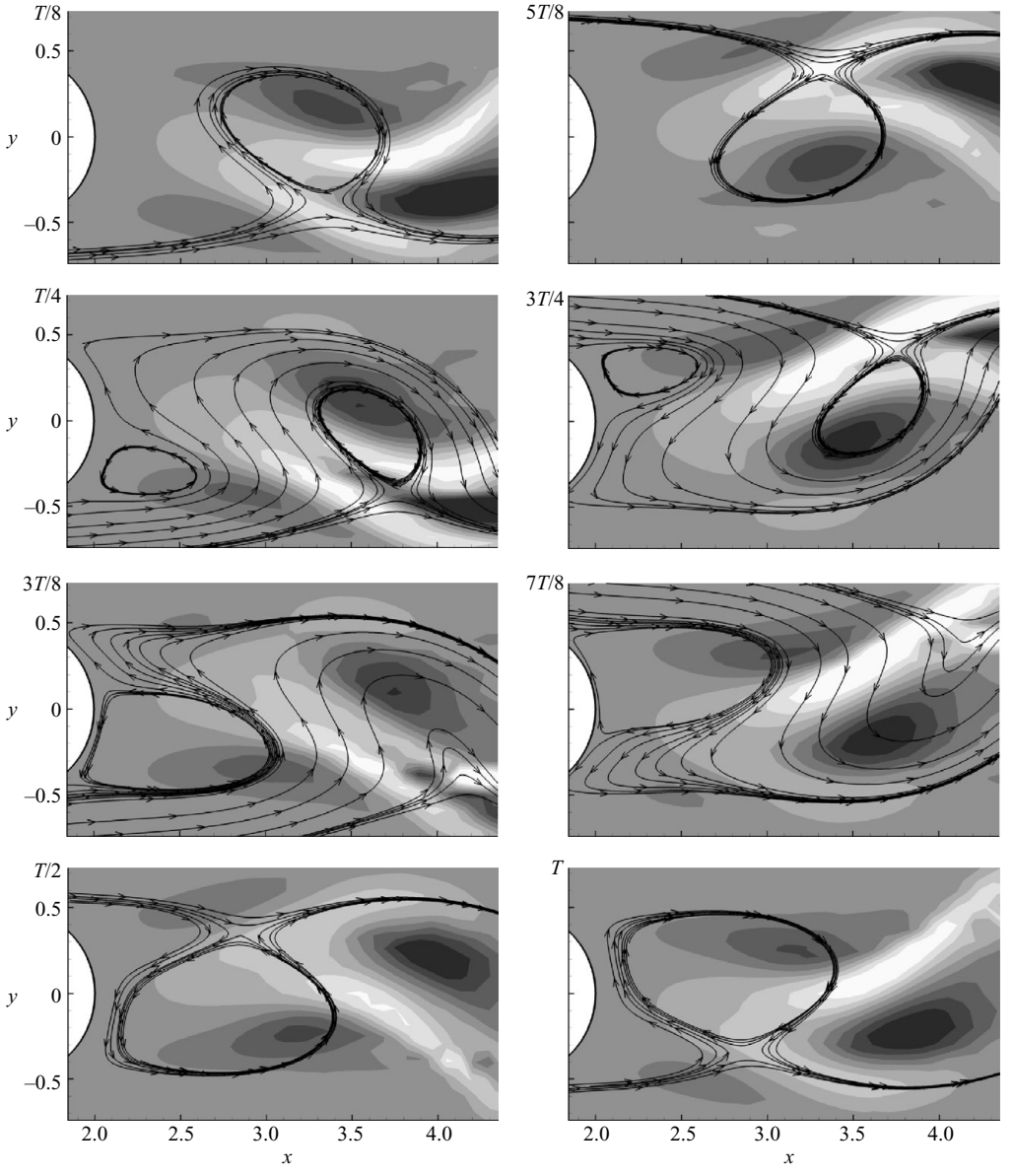

FIGURE 11. Base flow instantaneous streamtraces superposed to Floquet mode x vorticity at the base region of the downstream cylinder over one shedding period; $L_x/D = 1.5$, $Re = 315$, $\beta D = 2.998$ – mode T1. Light contours represent negative vorticity and dark contours represent positive vorticity.

of the wake. The process repeats symmetrically along the other half of the shedding period (instants $5T/8$ to T). The fact that the streamwise vorticity is amplified at one side of the wake, convected to the other side, amplified there and then convected back means that the sign of the streamwise vorticity observed in the wake does not change from one side of the wake to the other, and this explains the symmetry observed for this mode.

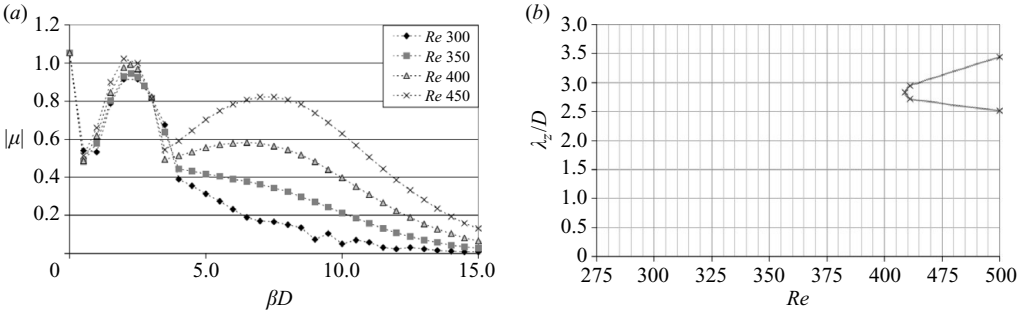

FIGURE 12. Flow around two circular cylinders in tandem with $L_x/D = 1.8$. (*a*) Modulus of Floquet multiplier as a function of the non-dimensional spanwise wavenumber, (*b*) neutral stability curves.

5.2. *Configuration* $L_x/D = 1.8$ – *shedding regime AG*

If the separation is increased so the shedding regime changes from *SG* to *AG* (see figure 4*b*), the secondary instability scenario also changes. In fact, two different transition modes are observed for regime *AG*; one for the smaller separations ($1.6 < L_x/D \leqslant 1.9$) and another for larger separations ($2.0 \leqslant L_x/D \leqslant 3.0$). In this section, the configuration $L_x/D = 1.8$ is used as a typical example to study the first mode in detail, while the second will be analysed in § 5.3.

5.2.1. *Linear analysis*

Figure 12 shows the variation of the modulus of the less stable Floquet multiplier with Reynolds number and perturbation wavenumber and also the neutral stability curve for this configuration. It can be seen in figure 12(*b*) that the flow becomes unstable for a larger Reynolds number ($Re_{cr} = 409 \pm 1$) than for the other cases. The wavenumber of the unstable mode at the onset is $\beta D = 2.214 \pm 0.002$, corresponding to a wavelength $\lambda_z/D = 2.838 \pm 0.003$, which is in between those of modes A and B observed in the flow around an isolated cylinder. This mode will be referred to as mode T2, and has a purely real Floquet multiplier. The least stable modes for higher wavenumbers ($\beta D \geqslant 4$) have complex Floquet multipliers.

Mode T2 streamwise vorticity contours superposed to base flow spanwise vorticity iso-lines for $Re = 415$ and $\beta D = 2.200$ are shown in figure 13. It can be seen that the symmetry of the mode x vorticity contours is the same as that of mode A for the isolated cylinder. It is worth noting that the Floquet mode streamwise vorticity contours are particularly strong in the shear layers of the base flow, unlike those of mode A. There is no evidence of spanwise flow in the gap between the cylinders, so we conclude that the instability originates in the near wake of the downstream cylinder, like mode T1. However, there is streamwise vorticity in the shear layers separating from the downstream cylinder even upstream of the region where the vortices are formed (see figure 20 for more clear evidence of spanwise flow in the base region of the downstream cylinder). This is different from mode T1, which originates further downstream, in the zone where the opposite shear layers interact.

5.2.2. *Nonlinear analysis*

The results for the nonlinear analysis of mode T2 displayed in figure 14 show a very unusual behaviour. The nonlinear growth of the perturbation follows the linear trend only for two or three cycles, and then the curve changes its slope drastically and starts to follow a much milder growth trend, as illustrated in figure 14(*b*). This

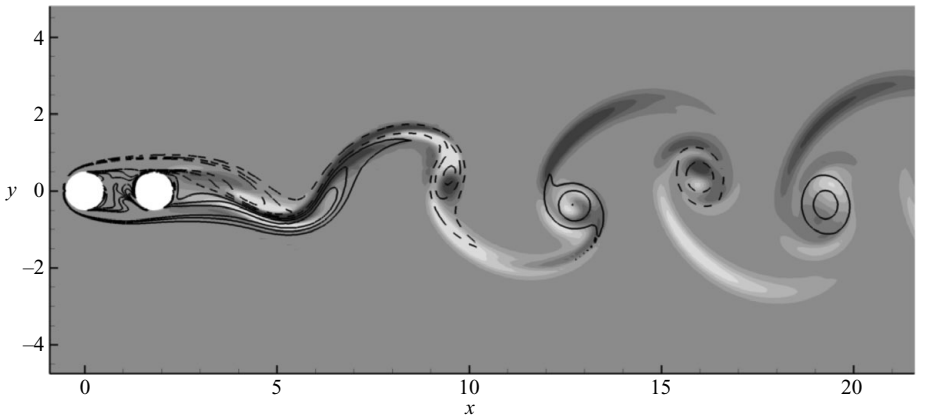

FIGURE 13. Mode T2 x vorticity contours and base z vorticity iso-lines, $L_x/D = 1.8$, $Re = 415$, $\beta D = 2.200$. Contours and lines are as in figure 8.

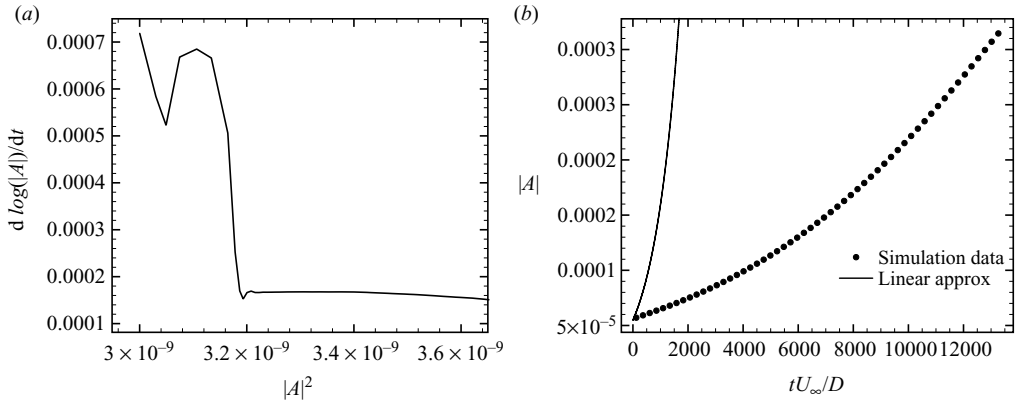

FIGURE 14. Results for three-dimensional nonlinear simulation of case $L_x/D = 1.8$, $Re = 415$, $\beta D = 2.2$ ($L_z/D = 2.856$) – mode T2. Axes and legends are the same as for figure 9.

is translated in the graph of d $\log(|A|)/\mathrm{d}t$ against $|A|^2$ in figure 14(a) as an initial decay, followed by an sharp transition to a state in which d $\log(|A|)/\mathrm{d}t$ evolves very slowly, corresponding to an almost flat curve in the graph. To confirm these results, we performed a number of tests which included increasing the resolution of the mesh, varying the Reynolds number in the vicinity of the bifurcation, decreasing the perturbation initial energy and decreasing the time step; all tests resulted in curves with the same behaviour.

As a tentative alternative approach to elucidate the nonlinear character of mode T2 bifurcation, additional calculations were performed to draw the diagram shown in figure 15. No hysteresis was observed, so the bifurcation could not be classified as subcritical. However, the square of the amplitude at saturation does not follow a straight line for Reynolds numbers higher than the critical either, and this rules out the classification of the bifurcation as supercritical.

Interestingly, although the perturbation energy grows in an unexpected way, the shape of the unstable mode is not altered significantly during the nonlinear evolution of the perturbation. The vorticity contours of the nonlinear calculations at saturation level are compared to a combination of the Floquet mode and base flow in figure 16.

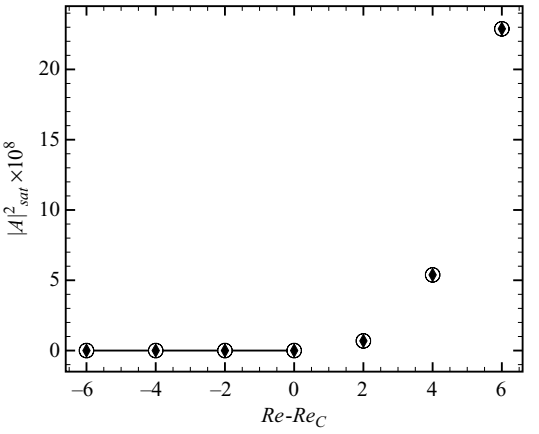

FIGURE 15. Bifurcation diagram for configuration $L_x/D = 1.8$, mode T2; ◯ – results for increasing Reynolds number, ◆ – results for decreasing Reynolds number.

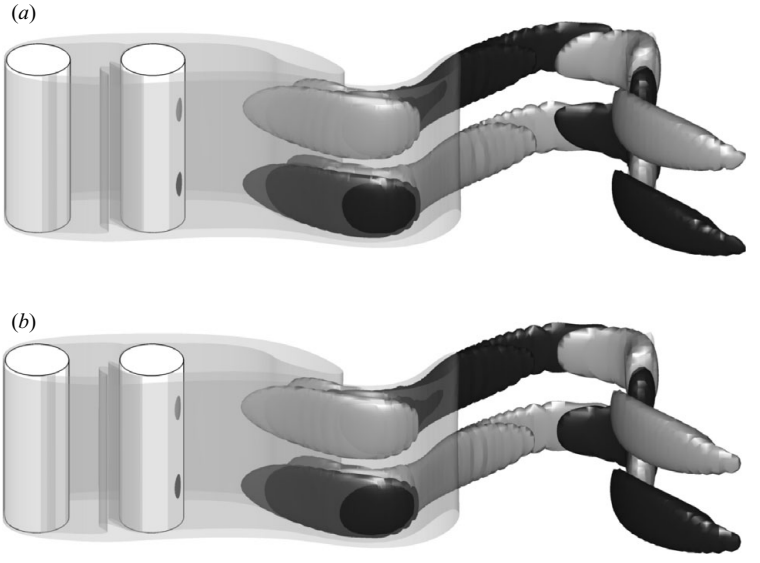

FIGURE 16. Three-dimensional views of the nonlinear results at the saturated state (*a*) and base flow combined with unstable Floquet mode (*b*), configuration $L_x/D = 1.8$, $Re = 415$, $\beta D = 2.2$ – mode T2. Surfaces are as in figure 10.

The plots refer to approximately the same phase of the shedding cycle. Like for $L_x/D = 1.5$, the structures of the Floquet mode can be plainly observed in the saturated state.

5.2.3. *Physical mechanism*

As seen in figure 13, mode T2 originates just after the leeward cylinder, in a region upstream from where the vortices are formed. This suggested that the mechanism responsible for the existence of the mode does not depend directly on the interaction between the shear layers, in the sense that it initiates at a region in which this interaction is absent. We confirmed this hypothesis by running stability calculations with a slightly modified geometry, placing a free-slip plate in the near wake of

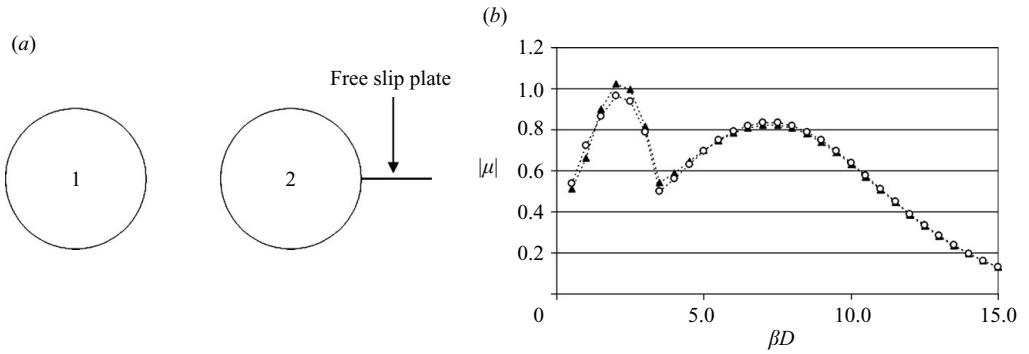

FIGURE 17. (*a*) Schematic drawing showing the free-slip plate used on additional stability calculations carried out to investigate the physical mechanism of mode T2. (*b*) Floquet multipliers obtained from the calculations with the free-slip plate (○), compared to the original results without the free-slip plate (▲), for $Re = 450$, $L_x/D = 1.8$.

the downstream cylinder, as illustrated in figure 17(*a*). The perturbation boundary conditions on this line were ($\partial u/\partial \boldsymbol{n} = 0$, $v = 0$, $\partial w/\partial \boldsymbol{n} = 0$). The original base flow (obtained without the free-slip plate) was utilized in the calculations. We argue that if the instability mechanism entails some sort of communication between the opposite sides of the wake, the presence of the plate should eliminate the mode. Figure 17(*b*) shows the results of this test: the values of the Floquet multiplier barely changed from those obtained with the original calculation. Therefore, it was concluded that the interaction between the shear layers does not play a role in the initiation of this mode. This contrasts with what is observed in all the other known three-dimensional modes in the flow around bluff bodies (for example, modes A, B, and QP), where the interaction between the shear layers seems to play an essential role in the inception of the instabilities.

Next, we present some evidence that suggests that mode T2 has its origin in a centrifugal instability at the near wake, and is amplified through a hyperbolical mechanism in the shear layers when the vortices are about to be shed. A centrifugal instability is a manifestation of an imbalance between centrifugal and viscous forces (Oertel 2004). The theoretical foundations of the centrifugal instability for viscous fluids were laid down by Taylor (1923), who also demonstrated this instability experimentally in the flow between two concentric cylinders. Bayly (1988) developed the basic principles of the centrifugal instability for generic convex closed streamlines, and showed that a necessary condition for centrifugal instability to occur in such flows is that the magnitude of the angular momentum should decrease in the outward direction. The centrifugal instability was later found to be the physical mechanism behind the three-dimensional instability of other steady flows such as the flow over a backward-facing step (Barkley, Gomes & Henderson 2002; Beaudoin *et al.* 2004).

The identification of a region susceptible to centrifugal instability using mathematical arguments is much more problematic for unsteady flows than for steady flows. However, in the present work the locations where the three-dimensional instabilities are stronger are given by the Floquet modes, so it is possible to check whether the base flow at these locations has certain characteristics that are found in steady flows prone to centrifugal instabilities. For example, Barkley *et al.* (2002) reported that, for the flow over a backward-facing step, the regions where the centrifugal instability was particularly strong were just behind the step edge and

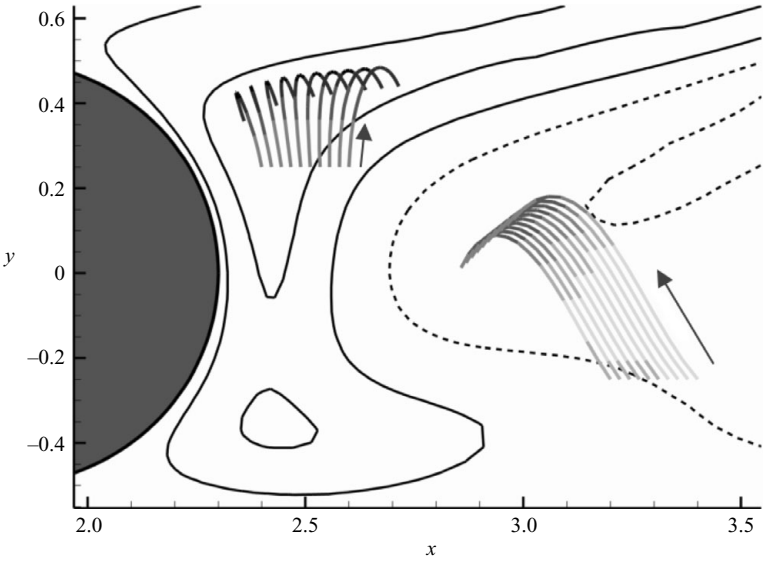

FIGURE 18. Base flow particle paths superposed to w contours of the Floquet mode, $L_x/D = 1.8$, $Re = 409$, $\beta D = 2.214$ – mode T2. The shades of grey of the path lines stand for the velocity magnitude along the path; light shades represent high velocities and dark shades represent low velocities; the arrows indicate the time sense of the paths.

at the downstream reattachment point. The common features of these regions are the significant curvature of the streamlines and strong deceleration of the flow. These characteristics make the gradient of the angular momentum in the direction away from the centre of curvature of the streamlines negative, with considerable magnitude. In the case of unsteady flow, particle paths should be used instead of streamlines. Figure 18 shows base flow particle paths superposed on the Floquet mode z velocity field; the time instant for which the mode is represented is the same as that when the particle paths were interrupted. The particles were released half a period earlier from rakes aligned in the x direction placed at convenient locations. In figure 18 the paths are drawn using shades of grey that represent the magnitude of the base flow velocity along the path. It can be seen that the regions where the mode spanwise velocity is greater are regions where the particle paths have large curvature and undergo significant deceleration.

The centrifugal instability produces the regions of y vorticity perpendicular to the axis of the cylinder, as shown in figure 19. In order to understand how this vorticity is transported to the wake and amplified, snapshots of the Floquet mode w contours at the base region of the leeward cylinder along a shedding period are displayed in figure 20. The figure shows that mode T2 exhibits two zones of opposite w velocity in the near wake of the downstream cylinder (a zone of positive w at the base region of the cylinder and a zone of negative w slightly more downstream) persisting through the entire period. Because of this, and because the x velocity of the base flow is predominantly negative in that same region, the combined flow displays persistent regions of y vorticity, which alternate in the spanwise direction (see figure 19). Due to the oscillation of the base flow in the y direction, these regions of y vorticity are transported towards the base flow shear layers (instants $T/8$ and $5T/8$ in figure 20). The shear layers are regions of strong gradient of U in the y direction, so the perturbation y vorticity is transformed to x vorticity through a tilting mechanism

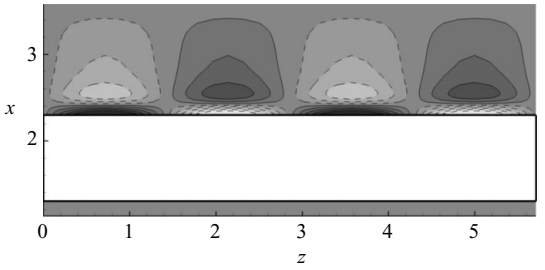

FIGURE 19. Contours of y vorticity at the $y=0$ plane for the three-dimensional simulation of the flow around configuration with $L_x/D=1.8$ at $Re=415$, showing mode T2. Light contours and dashed lines represent negative vorticity and dark contours and solid lines represent positive vorticity. Flow is from bottom to top.

(term $\omega_y'\partial U/\partial y$ in (2.8)). Since the y vorticity region at the base of the downstream cylinder has the same sign on both sides of the wake, but the base flow $\partial U/\partial y$ has a different sign on either side, the result is that the sign of the streamwise vorticity will be different on either side of the wake, and this determines the symmetry of mode T2. This change of sign in the streamwise vorticity is illustrated in figure 20. When streamwise vorticity appears in the shear layer with negative spanwise vorticity (the shear layer separating on the top of the cylinder in the figure), the region of spanwise velocity that is closer to the cylinder will be at the top (instant $T/4$). On the other hand, when y vorticity is transformed in x vorticity in the shear layer with positive spanwise vorticity, the region of spanwise velocity that is closer to the cylinder will be at the bottom (instant $3T/4$).

A little further downstream, in the region where the opposite shear layers interact to form the vortices, the perturbation w velocity is strengthened, as can be seen in the snapshots corresponding to the instants $T/2$ and T in figure 20. The rationale behind this is that when the streamwise vortex reaches the edge of the vortex formation region, which is a zone of hyperbolic flow (figure 21), the streamwise vorticity is amplified through a stretching mechanism, in an analogous way to the mechanism described for mode T1. These regions where the x vorticity is amplified are those where the contours are more evident in figure 13.

5.3. *Configuration $L_x/D=2.3$ – shedding regime AG*

When the gap space was increased a little further, but not enough to alter the base flow shedding regime, another change in the onset of the three-dimensional transition was observed. The configuration with $L_x/D=2.3$ was chosen to illustrate this scenario because the shedding regime and secondary instability character did not change over a significant Reynolds number range ($200\leqslant Re\leqslant 350$).

5.3.1. *Linear analysis*

The results for the modulus of the Floquet multiplier are shown in figure 22(*a*). For $Re=200$, the flow is stable. It then becomes neutrally stable at $Re=250\pm1$ with a wavenumber of $\beta D=1.366\pm0.02$ ($L_z/D=4.600\pm0.007$), and is unstable for higher Reynolds numbers. Only one unstable mode appears for $Re\leqslant 350$, and the non-dimensional wavenumber of maximum growth of this mode, which will be called mode T3 and has purely real Floquet multiplier, is approximately $\beta D=1.32$. For $\beta D\geqslant 3.5$, the least stable modes always had complex Floquet multipliers.

The neutral stability curve drawn in figure 22(*b*) shows that the wavelength range of this mode expands quickly with the Reynolds number, and at $Re=350$ it spreads

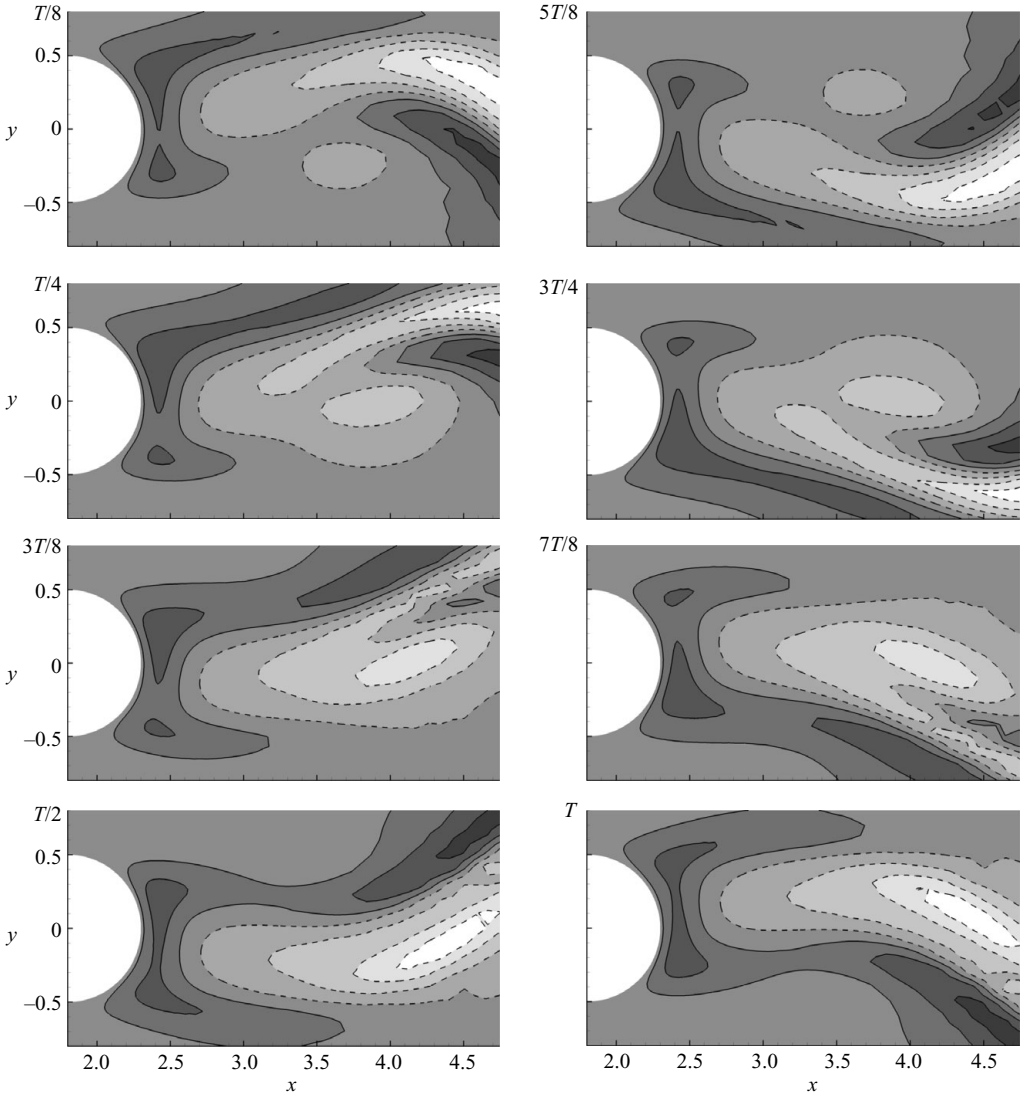

FIGURE 20. Snapshots of Floquet mode contours of z velocity at the base region of the downstream cylinder along one shedding period, $L_x/D = 1.8$, $Re = 409$, $\beta D = 2.214$ – mode T2. Light contours and dashed lines represent negative velocity and dark contours and solid lines represent positive velocity.

from $\lambda_z/D = 3.16$ to $\lambda_z/D = 11.9$. The critical Reynolds number for this configuration is lower than those for $L_x/D = 1.5$ and $L_x/D = 1.8$, but still considerably higher than that for the single cylinder case, and the wavenumber of mode T3 at the bifurcation is slightly smaller than the single cylinder mode A wavenumber $\beta D = 1.587$.

The shape of mode T3 is depicted in figure 23. It can be seen that this instability originates in the gap region, hence differing from modes T1 and T2, both of which first appeared behind the downstream cylinder. Figure 23 also shows that the instability observed for $L_x/D = 2.3$ breaks the spatial symmetry of the base flow, presenting x vorticity of the same sign on both sides of the wake, as in the single cylinder mode B.

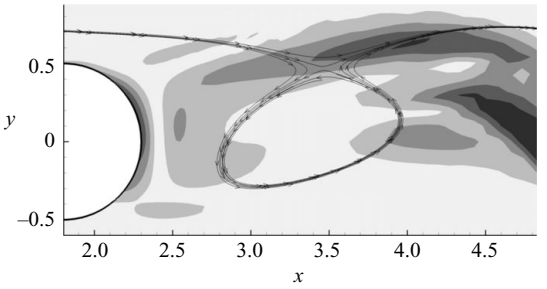

FIGURE 21. Base flow instantaneous streamtraces superposed to Floquet mode magnitude of vorticity in the plane xy ($\omega_{xy} = \sqrt{\omega_x^2 + \omega_y^2}$), showing amplification of streamwise vorticity in a region of hyperbolic flow for mode T2. $L_x/D = 1.8$, $Re = 409$, $\beta D = 2.214$.

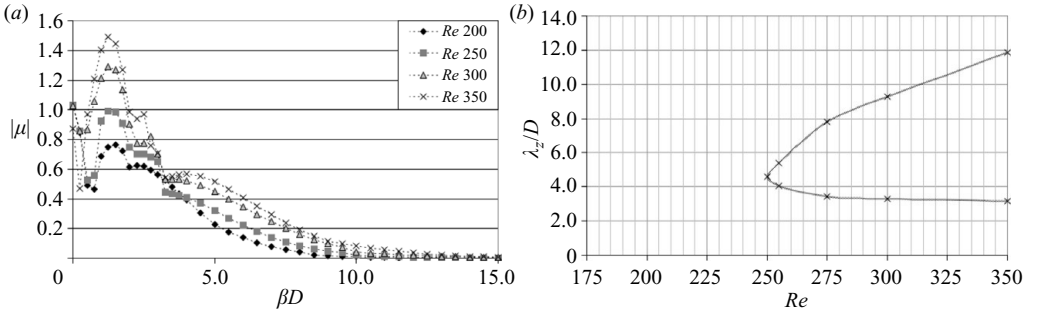

FIGURE 22. Flow around two circular cylinders in tandem with $L_x/D = 2.3$. (a) Modulus of Floquet multiplier as a function of the non-dimensional spanwise wavenumber, (b) neutral stability curves.

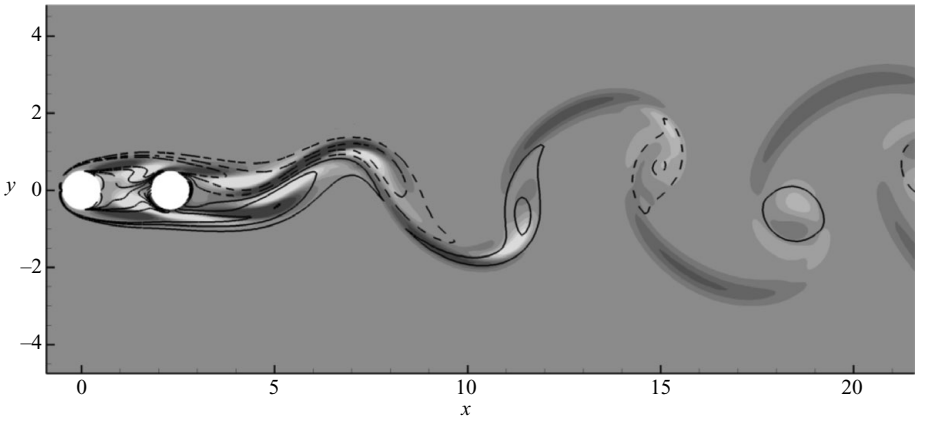

FIGURE 23. Mode T3 x vorticity contours and base z vorticity iso-lines, $L_x/D = 2.3$, $Re = 255$, $\beta D = 1.37$. Contours and lines are as in figure 8.

5.3.2. *Nonlinear analysis*

Figure 24 shows the results of the nonlinear analysis for this configuration. As in the configuration $L_x/D = 1.5$, the bifurcation of the mode is clearly supercritical and the Landau equation truncated at the third-order models the bifurcation very well. The bifurcation diagram in the inset of figure 24(b) also confirms that the bifurcation

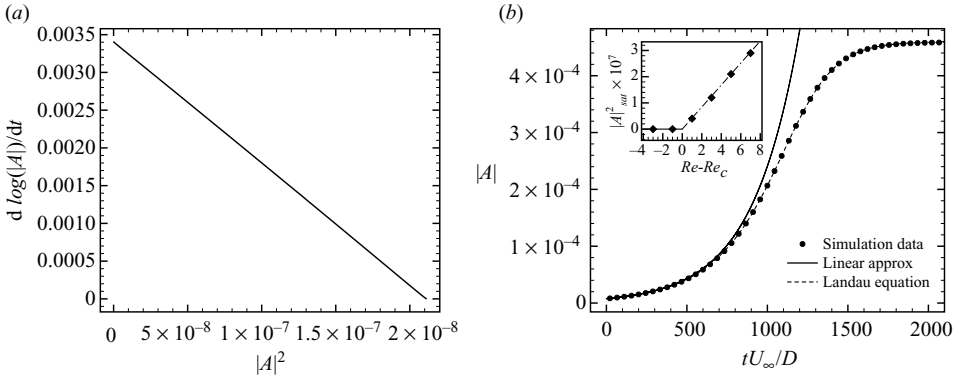

FIGURE 24. Results for three-dimensional nonlinear simulation of case $L_x/D = 2.3$, $Re = 255$, $\beta D = 1.37$ ($L_z/D = 4.586$) – mode T3. Axes and legends are the same as for figure 9.

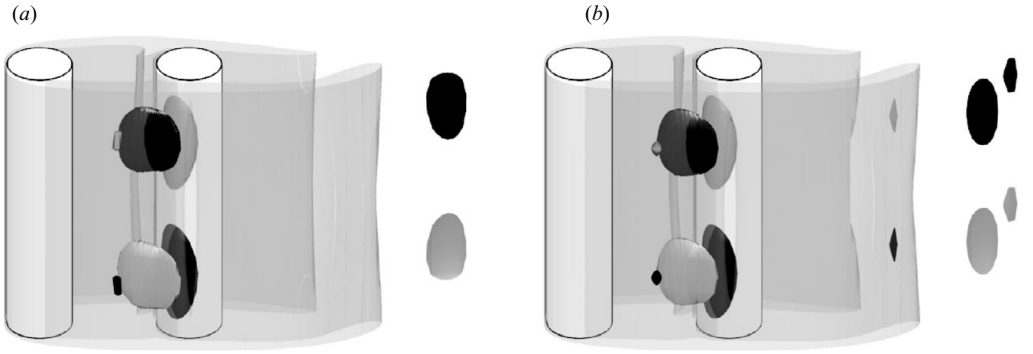

FIGURE 25. Three-dimensional views of the nonlinear results at the saturated state (*a*) and base flow combined with unstable Floquet mode (*b*), configuration $L_x/D = 2.3$, $Re = 255$, $\beta D = 1.37$ – mode T3. Surfaces are as in figure 10.

is supercritical. Another similarity to the configuration $L_x/D = 1.5$ is the fact that the three-dimensional structures of the unstable mode are evident in the saturated state of the nonlinear simulations (figure 25).

5.3.3. *Physical mechanism*

The physical mechanism that drives mode T3 shows a number of similarities with the short wavelength instability of a pair of counter-rotating vortices. According to Leweke & Williamson (1998*a*), who investigated the stability of this flow using experiments in a water tank, this instability has an elliptic nature (Bayly 1986; Pierrehumbert 1986) and due to a kinematic matching condition for the disturbances evolving on each vortex core, this instability develops in a cooperative manner. Billant, Brancher & Chomaz (1999) presented a numeric three-dimensional stability analysis of a counter-rotating vortex pair. They observed two unstable short wavelength modes in their calculations; one symmetric and one antisymmetric. The antisymmetric mode had the larger growth and the authors used this fact to explain why this was the only short wavelength mode observed in the experiments of Leweke & Williamson (1998*a*).

The transient nature of the wake vortices, the existence of a free stream of relatively large magnitude and the presence of the cylinders very close to the vortices in the

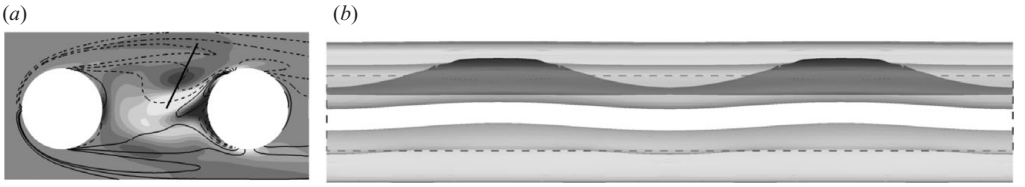

FIGURE 26. (*a*) Contours of perturbation spanwise vorticity superposed to base flow vorticity iso-lines, $L_x/D = 2.3$, $Re = 255$, $\beta D = 1.370$ – mode T3. The perturbation spanwise vorticity forms a dipole which is aligned in the direction of the stretching, indicated by the solid thick line. (*b*) λ_2 iso-surfaces for the saturated state of the three-dimensional simulation, $L_x/D = 2.3$, $Re = 255$, showing the vortices immediately upstream of the leeward cylinder (for the definition of the λ_2 criterion of vortex identification see Jeong & Hussain 1995). The transparent light grey surfaces represent surfaces where $\lambda_2 = -0.1$ and solid dark grey surfaces represent surfaces where $\lambda_2 = -0.8$. The downstream cylinder is represented by the dotted lines.

current results are very important differences from pure vortex flows, and these differences should be kept in mind when drawing any comparison between the two. However, there are some similarities between our results and those obtained for pure vortex flows which suggest that the physical mechanism that sustains mode T3 and the cooperative elliptical instability in a pair of counter-rotating vortices is the same. First, in both cases there are two counter-rotating vortices in close proximity interacting with each other. We also noticed that the symmetry of both modes is the same, if we consider the instants of maximum spanwise vorticity in the base flow:

$$[u, v, w](x, y) = [-u, v, -w](x, -y),$$
$$[\omega_x, \omega_y, \omega_z](x, y) = [\omega_x, -\omega_y, \omega_z](x, -y).$$

In addition, similarly to the cooperative elliptical instability, mode T3 exhibits a spanwise vortex dipole within the vortex cores, and those regions are aligned with the stretching direction, as shown in figure 26(*a*).

However, there are also differences between mode T3 and the results for a pair of counter-rotating vortices previously published in the literature. The first is the wavelength of the perturbation, which is of the order of the vortex core for the pure vortex pair (Leweke & Williamson 1998*a*) and varies from $4.25D$ to $10.0D$ at the onset for mode T3, depending on the geometry considered, as will be discussed in § 6. If we consider that the cores of the vortices in the wake have approximately the same diameter as the cylinders, this means that the wavelength of mode T3 is considerably larger. Another difference is the fact that Leweke & Williamson (1998*a*) and Billant *et al.* (1999) reported that the waviness of the inner and outer layer of the vortex cores had opposite signs. This is not the case for mode T3, as can be seen in figure 26(*b*); in the current results, the inner and outer layers bent in phase. These discrepancies might be justified by the remarkable difference between the strain fields and vortex cores of the two cases. For the classic counter-rotating vortex pair, the strain field and the core size are almost steady, changing slowly as the vortices are deformed. On the other hand, in the flow around circular cylinders in tandem, both the strain field and size of the cores are time-dependent and affected by the solid walls in great measure.

In order to obtain additional evidence to support the hypothesis that these two instabilities have the same origin, we ran an additional set of stability calculations on a slightly modified geometry. The stability of the base flow obtained for the configuration with $L_x/D = 2.3$ at $Re = 300$ was tested to three-dimensional perturbations with an additional constraint. A free-slip plate of $0.5D$ aligned with the

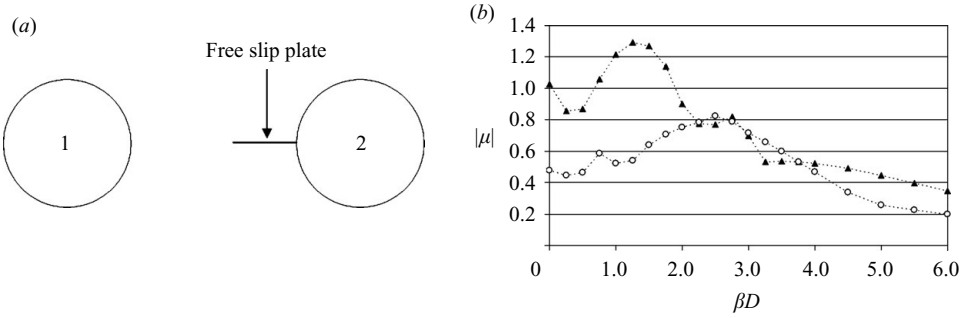

FIGURE 27. (*a*) Schematic drawing showing the free-slip plate used on additional stability calculations carried out to investigate the physical mechanism of mode T3. (*b*) Floquet multipliers obtained from the calculations with the free-slip plate (○), compared to the original results without the free-slip plate (▲), for $Re = 300$, $L_x/D = 2.3$.

line that passes through the centres of the cylinders was placed at the upstream end of the downstream cylinder, as illustrated in figure 27(*a*). The perturbation boundary conditions on this line were ($\partial u/\partial \boldsymbol{n} = 0$, $v = 0$, $\partial w/\partial \boldsymbol{n} = 0$). The rationale behind this test was that if T3 instability had a cooperative nature, the imposition of this free-slip plate should hinder its growth, since the communication between the two vortices on the opposite sides of the wake would be prevented. As can be seen in figure 27(*b*), this was indeed observed. The Floquet multipliers in the range in which mode T3 is unstable in the original calculations ($1.5 \lesssim \beta D \lesssim 2.0$) are all stable for the modified case and there is not even a local peak in the curve of the modified case. For higher wavenumbers, the results of the modified case roughly follow the original results. Therefore, it seems that mode T3 has the same nature as the cooperative elliptical instability of counter-rotating vortex pairs, and the few dissimilarities between the two instabilities can be accounted for by the differences in the base flows.

5.4. *Configuration $L_x/D = 5$ – shedding regime WG*

If the separation is further increased, the vortex shedding regime eventually changes. The flow around the configuration with $L_x/D = 5$ is an example of the vortex shedding regime *WG*, in which a complete von Kármán wake can be observed in between the cylinders (see figure 4*c*).

5.4.1. *Linear analysis*

Figure 28(*a*) shows the results for $L_x/D = 5$, which are very similar to the results observed for the flow around a single cylinder. There are two noticeable peaks: one for low wavenumber and one for high wavenumber. The Floquet multiplier is real and positive at both peaks and, in the flow around a single cylinder, they correspond to modes A (low β) and B (high β) (Barkley & Henderson 1996). Also similar to the single cylinder case is the fact that the least unstable modes for intermediate wavenumbers (between the two peaks) have complex Floquet multipliers.

The neutral stability curves displayed in figure 28(*b*) also bear a strong resemblance to those for a single cylinder. However, the long wavelength critical Reynolds number for $L_x/D = 5.0$ is 180 ± 1, which is lower than that for mode A in the single cylinder, and the wavenumber of the unstable mode at the bifurcation, $\beta D = 1.662 \pm 0.002$, is slightly larger than that of mode A. On the other hand, the short wavelength mode becomes linearly unstable later in Re terms for the tandem arrangement

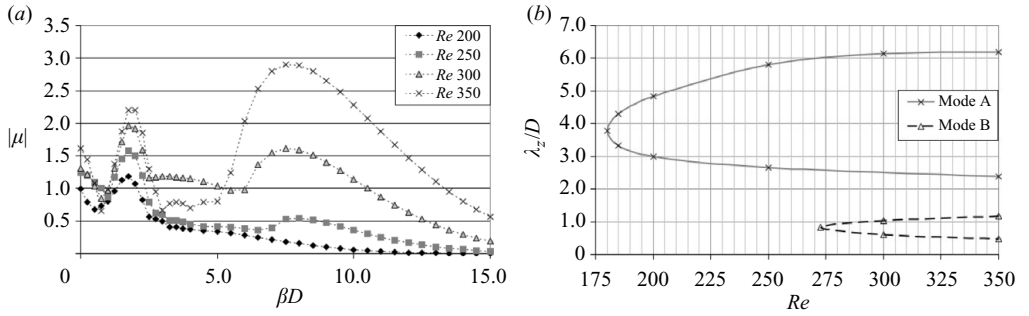

FIGURE 28. Flow around two circular cylinders in tandem with $L_x/D = 5$. (*a*) Modulus of Floquet multiplier as a function of the non-dimensional spanwise wavenumber, (*b*) neutral stability curves.

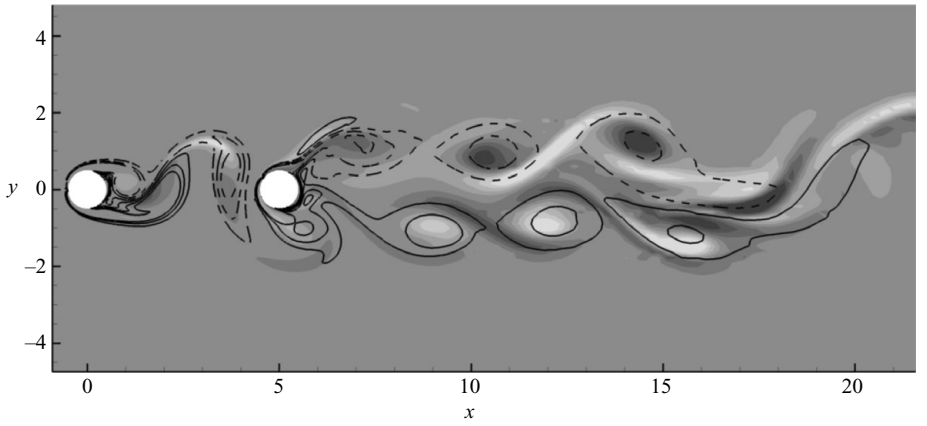

FIGURE 29. Floquet mode x vorticity contours and base z vorticity iso-lines, $L_x/D = 5$, $Re = 200$, $\beta D = 1.75$ – mode A. Contours and lines are as in figure 8.

($Re_{cr} = 272.5 \pm 1$) than for mode B in the single cylinder case, and the wavelength of the unstable mode $\beta D = 0.823 \pm 0.002$ coincides with that of mode B.

The low wavenumber mode is already unstable for $Re = 200$. Looking at the streamwise vorticity contours in figure 29, it can be seen that, like mode A, this mode maintains the base flow symmetry. Given all the similarities between the present mode and the single cylinder mode A (wavenumber, symmetry, critical Re), we argue that these instabilities are indeed of the same type. Also in figure 29, we see that the perturbation originates in the near wake of the upstream cylinder and gets stronger when it impinges on the downstream cylinder. Further downstream, in the region where the vortices interact in the far wake, the instability is again amplified, as also reported in Carmo *et al.* (2008).

In fact, this behaviour appears to be consistent with the hypothesis that mode A is a manifestation of elliptic instability of the vortex cores (Williamson 1996; Leweke & Williamson 1998*b*; Thompson, Leweke & Williamson 2001). According to this hypothesis, the deformation of the vortex cores, which makes them assume an elliptical form, and the interaction between the vortex cores due to their proximity are key factors in initiating and sustaining mode A. It appears that the presence of the downstream cylinder favours both the deformation and the interaction of the vortex

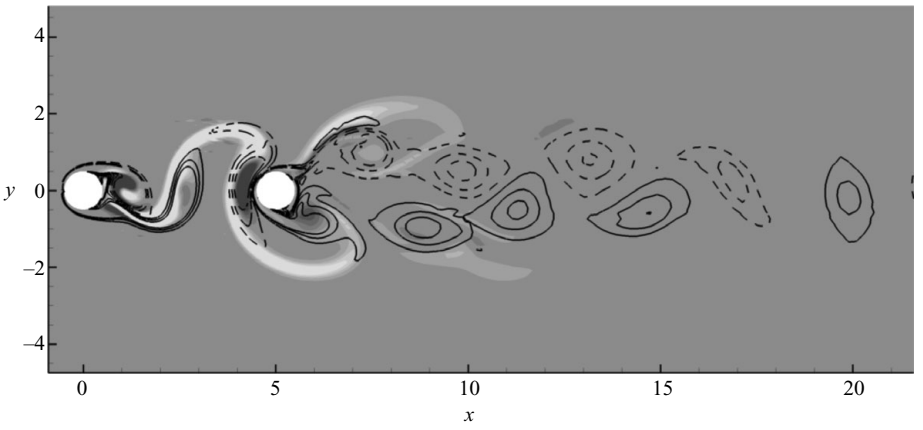

FIGURE 30. Floquet mode x vorticity contours and base z vorticity iso-lines, $L_x/D = 5$, $Re = 300$, $\beta D = 8.0$ – mode B. Contours and lines are as in figure 8.

cores in different regions of the flow field. First of all, the presence of the downstream cylinder generates an adverse pressure gradient in the interstitial region (Carmo & Meneghini 2006), which is expected to enhance the deformation and interaction of the cores in the near wake of the upstream cylinder. Since mode A instability is initiated in the near wake of the upstream cylinder, this feature may explain why this mode becomes unstable earlier in terms of Reynolds number for flows around tandem arrangements in regime *WG* than for the flow around an isolated cylinder. When the vortices approach and impinge on the downstream cylinder, they undergo considerable deformation and merge with the shear flow developing close to the surface of the cylinder, and this seems to favour mode A instability. Lastly, the wake formed after the downstream cylinder consists of strong large vortices that interact vigorously at a certain distance downstream, provoking further deformation of the vortex cores and strengthening the mode A contours, as illustrated in figure 29.

Figure 30 shows the unstable mode streamwise vorticity contours for the high wavenumber instability. We observed that the instability has the same nature as mode B, with the same symmetry, and a similar wavenumber and critical Reynolds number. Furthermore, the streamwise vorticity is concentrated in the shear layers that link the vortex cores. Unlike mode A, mode B instability gets weaker when it reaches the downstream cylinder and is absent in the region of vortex interaction in the far wake. This suggests that mode B instability in its linear stage is concentrated in and strongly depends on the shear layers that link the vortex cores. Since the shedding from the downstream cylinder is triggered by the vortices impinging on it, and not by the interaction between the two opposite shear layers as happens in the near wake of the upstream cylinder, the shear layers are much weaker in the far wake. This is also consistent with most of (if not all) previously proposed physical mechanisms for the origin of mode B (see e.g. Brede, Eckelmann & Rockwell 1996; Williamson 1996; Ryan, Thompson & Hourigan 2005), all of those have stated that mode B instability originates and develops in the shear layers.

5.4.2. *Nonlinear analysis*

The nonlinear analysis of the bifurcations that were observed for $L_x/D = 5$ faced an additional difficulty, because the interaction of the detached vortices with the downstream cylinder and the interaction between the vortices in the far wake made

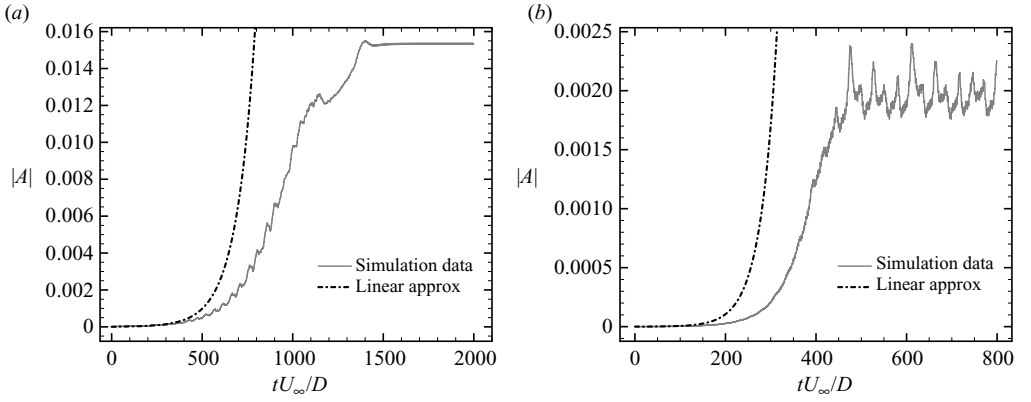

FIGURE 31. Results for three-dimensional nonlinear simulations of configuration $L_x/D = 5.0$, showing the growth and saturation of the perturbation amplitude and the growth predicted by linear stability analysis. The x-axis is non-dimensional time: (a) displays the evolution of mode A, at $Re = 185$ and $\beta D = 1.66$ ($L_z/D = 3.785$); (b) displays the evolution of mode B, at $Re = 278$ and $\beta D = 7.57$ ($L_z/D = 0.83$).

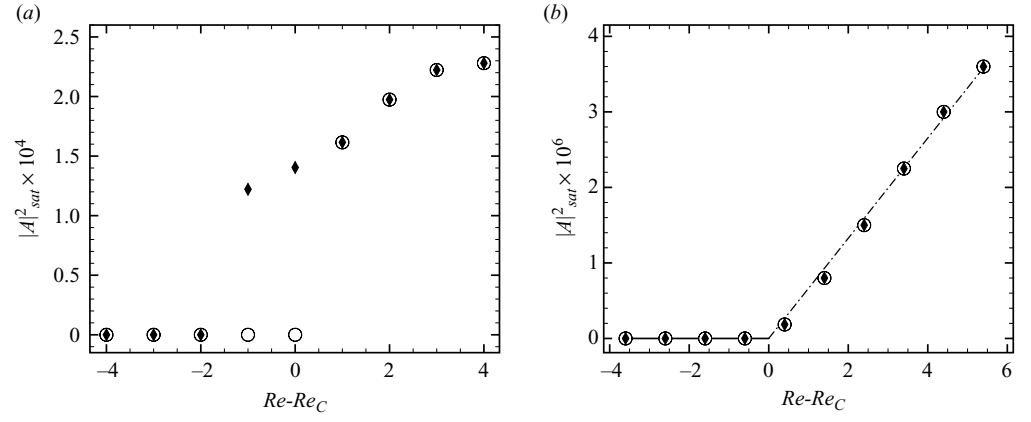

FIGURE 32. Bifurcation diagrams for configuration $L_x/D = 5$, showing a subcritical bifurcation for mode A (a) and a supercritical bifurcation for mode B (b); ○ – results for increasing Reynolds number, ◆ – results for decreasing Reynolds number.

the two-dimensional flow non-periodic outside the near wake of the upstream cylinder. As a result, the perturbation energy evolution curves were not smooth, as can be seen in figure 31, and the coefficients of the Landau equation could not be obtained from the graphs of $\mathrm{d}\,log|A|/\mathrm{d}\,t$ versus $|A|^2$.

However, the character of the bifurcations for modes A and B can be inferred from the bifurcation diagrams in figure 32, which display the amplitude squared of the perturbation at Reynolds numbers in the vicinity of the critical value for transition. For mode A, the results in figure 32(a) show hysteretical behaviour, which is a sign of subcritical bifurcation. In contrast, the results obtained for mode B, displayed in figure 32(b), show a diagram typical of a supercritical bifurcation, with no hysteresis and the values of the amplitude squared of the perturbation following a straight line after the bifurcation. Therefore, the nonlinear characteristics of the bifurcations for

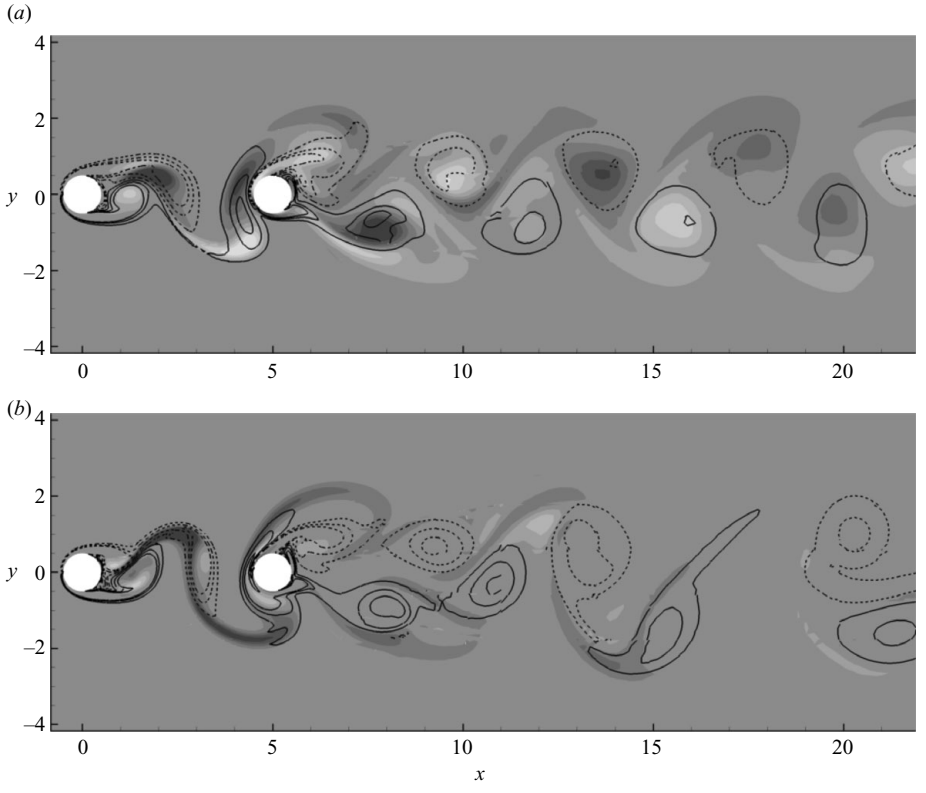

FIGURE 33. z vorticity iso-lines and x vorticity contours at xy planes showing the saturated state of the nonlinear perturbation evolution for modes A and B, $L_x/D = 5$. Non-dimensional values of z vorticity vary from –2.2 (dashed lines) to 2.2 (continuous lines) and non-dimensional values of x vorticity vary from –1.1 (light contours) to 1.1 (dark contours). (*a*) Mode A: $Re = 185$, $\beta D = 1.660$ ($L_z/D = 3.785$). Slice at $z = 0.85$. (*b*) Mode B: $Re = 278$, $\beta D = 7.57$ ($L_z/D = 0.83$). Slice at $z = 0.2$.

modes A and B observed for tandem arrangements with large separations are the same as those observed in the flow around a single cylinder (Henderson 1997).

Another interesting aspect of the nonlinear evolution of the perturbation can be seen in the graphs displayed in figure 31. There is a remarkable difference between the behaviour of the amplitudes of modes A and B when they reach the saturation level. While the energy associated to mode A reaches an approximately steady level at saturation, mode B shows large oscillations around a fixed mean value. The reasons for these behaviours can be understood by looking at the contour plots of these saturated states in figure 33. For mode A (figure 33*a*), the vortex cores become structures with strong three-dimensional characteristics due to the action of the instability in these regions. As a consequence, the vorticity in the spanwise direction becomes weaker and the correlation of the flow in the spanwise direction smaller. This hinders the interaction between the vortices in the far wake of the two-dimensional simulations at the same Reynolds numbers (see the iso-lines of figure 29). Interestingly, this results in a conspicuously regular wake which can be observed in the three-dimensional simulations, and this regularity is reflected in the steady level of energy of the saturated perturbation observed in figure 31(*a*). For mode B, on the other hand, even after the perturbation reaches saturation, the vortex cores in the far

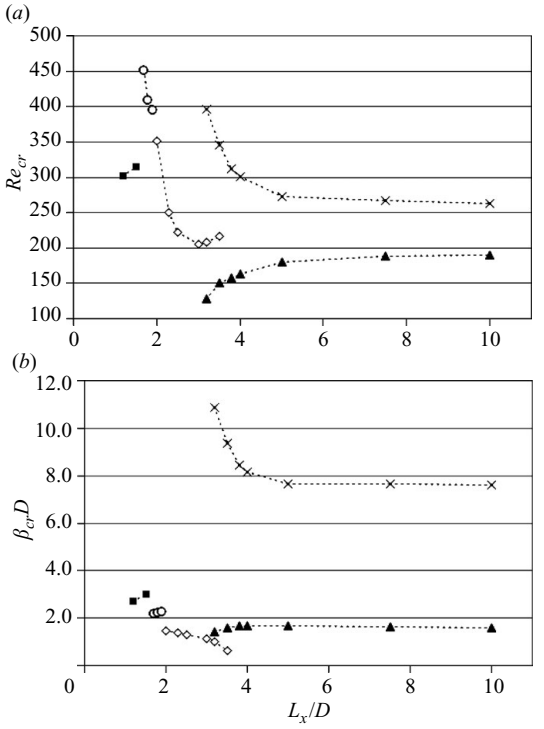

FIGURE 34. Variation of the critical Reynolds numbers (*a*) and respective perturbation wavenumbers (*b*) with the centre-to-centre separation for modes T1 (■), T2 (○), T3 (◇), A (▲) and B (×). Mode T1 bifurcates from shedding regime *SG*, modes T2 and T3 from shedding regime *AG* and modes A and B from shedding regime *WG*.

wake are approximately two-dimensional, because the instability evolves and remains restricted to the shear layers that link the cores, (see figure 33*b*). Therefore, the cores have spanwise vorticity strong enough to sustain the interaction and merging that occurs in the far wake, resulting in a chaotic flow. This irregular behaviour is also displayed in the perturbation energy plotted in figure 31(*b*).

6. Discussion

6.1. *Dependence of the critical Reynolds number and unstable mode wavenumber on the centre-to-centre separation*

In order to present a more complete picture of how the onset of the three-dimensional wake instabilities varied according to the cylinder separations, the critical Reynolds numbers and respective perturbation wavenumbers of additional configurations were calculated and are plotted in figure 34. Due to the hysteresis in the transition between the base flow shedding regimes *AG* and *WG*, it is possible to observe two different transition scenarios in the range $3 \leqslant L_x/D \leqslant 4$, depending on how the base flow was obtained. The mode T3 curve refers to base flows obtained by restarting the simulations from lower Reynolds numbers results, so the base flow shedding regime was *AG*. In contrast, the curves of modes A and B in this separation range refer to base flows obtained by restarting the simulations from higher Reynolds number simulations, resulting in shedding regimes *WG*. Hysteresis was also observed in the

transition between the shedding regimes *SG* and *AG*. However, it was not possible to obtain the bifurcation points of flows with regime *AG* for $L_x/D \leqslant 1.5$, because the critical Reynolds number was not inside the range for which this shedding regime exists for these configurations. The same applies for flows with regime *SG* for $L_x/D \geqslant 1.7$. The flow around the configuration $L_x/D = 1.6$ was very unstable, constantly shifting the shedding regime between *SG* and *AG*, rendering the calculation of any bifurcation point impracticable.

For configurations with shedding regime *SG*, whose secondary instability is mode T1, the critical Reynolds number increased with increasing separation. A possible explanation for this behaviour is that when the separation is increased, the shear layers become more elongated and more vorticity remains trapped in the gap between the cylinders. Consequently, the shear layers will be less energetic at the formation region, where the three-dimensional instabilities originate.

When the separation was increased further, the shedding regime became *AG* and the first three-dimensional instability was mode T2. For such flows, the critical Reynolds number decreased for increasing separation. This decrease seems to be caused by the fact that the vortex formation region approaches the downstream cylinder for increasing separations; hence the backflow zone between the cylinder and the vortex formation region becomes more compact. As discussed in § 5.2.3, this backflow zone is where the centrifugal instability takes place. When this zone is more compact, the flow in there is likely to be subjected to higher curvatures and decelerations, thus facilitating the initiation of the instability.

For separations which are even larger, although not so large as to lead to a change of base flow shedding regime, the three-dimensional instability modifies to mode T3. For this mode, the critical Reynolds number initially decreases for increasing separation, and then slightly increases for the separations in the range of transition between shedding modes *AG* and *WG*. Considering that the instability originates in the gap between the cylinders, the decrease in the critical Reynolds number for separations smaller than those in the transition range is not surprising, since more vorticity remains in the interstitial region if the separation is increased, making the vortices stronger and larger in this region. This also explains why the unstable mode wavenumber decreases for mode T3, since the mode wavelength scales with the size of the cores.

For flows in shedding regime *WG*, the results displayed in figure 34(*a*) confirm that for small L_x/D within this range, mode A bifurcates earlier in terms of Reynolds number than it does for the isolated cylinder, and mode B bifurcates later. These results reinforce the arguments put forwards in § 5.4 regarding the physical mechanisms of these modes. If the separation is increased, the values of critical Reynolds number for modes A and B quickly converge to those obtained in the flow around an isolated cylinder, and for $L_x/D \geqslant 10$ there are no significant differences in the critical Reynolds numbers and perturbation wavenumber at the onset between the results obtained for the single cylinder and those obtained for tandem arrangements, within 1 % tolerance. The unstable mode wavenumbers are also very close to those of the isolated cylinder for separations larger than those in the drag inversion range.

The stability analysis results regarding the critical Reynolds number for flows in regimes *SG* and *AG* clarify the conclusions of Deng *et al.* (2006). Deng *et al.* stated that the transition to three-dimensional flow in the wake arose later in terms of Reynolds number in comparison to the single cylinder case, when the separation between the cylinders was less than the separation at which the drag inversion occurs. The same was observed by Papaioannou *et al.* (2006), who also noticed that for

separations larger than the drag inversion spacing, the downstream cylinder had a destabilizing effect. This is in line with the stability results presented here, since the critical Reynolds number for mode A was lower for the tandem arrangements with shedding regime *WG* than for a single cylinder.

6.2. *Equivalence of modes based on the physical mechanism*

Secondary instabilities in the wake of flows around bluff bodies have been widely studied (Barkley & Henderson 1996; Sheard, Thompson & Hourigan 2003; Blackburn *et al.* 2005; Carmo *et al.* 2008 and others). Since these flows have many points in common, it is worth investigating whether any observed new mode is a manifestation of a previously studied instability. This is not a trivial exercise, because the similarities between modes observed in the wakes of distinct configurations may be obscured by the differences in the base flows. The common ground that should be used for this kind of comparison is the physical mechanism that initiates the instabilities. In the cases presented in this paper, it appears that mode T1 can be understood as a manifestation of mode B and mode T3 as a manifestation of mode A. It was not possible to relate mode T2 to any previously published mode known to the authors, apart from the three-dimensional mode found by Barkley *et al.* (2002) in the flow over a backward-facing step .

When comparing mode T1 to mode B, we have to take into account that the physical mechanism responsible for mode B is still a matter of controversy. While some researchers advocate that this mode stems from a centrifugal instability (Brede *et al.* 1996; Blackburn & Lopez 2003; Ryan *et al.* 2005), others suggest that mode B originates from a hyperbolic instability (Williamson 1996; Leweke & Williamson 1998*b*). In fact, it is extremely difficult to distinguish one mechanism from the other because of the topology of the flow in the near wake: there is a hyperbolic flow region in the vicinity of a vortex. A hyperbolic region has a stagnation point in its middle. The presence of a stagnation point close to a vortex implies that the angular momentum will decay towards this stagnation point, and this is favourable to the onset of centrifugal instability. Therefore, the initiation of an unstable mode in this region is likely to be interpreted as a manifestation of either of these instabilities.

The mechanism we observed for mode T1 has many points in common with that suggested by Williamson (1996) and Leweke & Williamson (1998*b*) to explain the origin and sustainment of mode B. The only significant difference is that we could not identify any 'imprinting' and amalgamation mechanism in line with that proposed by Williamson (1996) to explain the symmetry of the mode. Instead, we observed that the streamwise vorticity was advected by the base flow from one side of the wake to the opposite side and upstream. This was followed by an amplification of streamwise vorticity due to vortex stretching in another region of hyperbolic flow. This mechanism is satisfactorily supported by the perturbation vorticity equations (2.6) and (2.7). In addition, it also explains the experimental observations by Brede *et al.* (1996), who reported that mode B showed simply connected areas of streamwise vorticity. Given the notable number of similarities between modes T1 and B, we contend that these modes are indeed the same.

Mode A is proposed to be an instability of elliptical type (Williamson 1996; Leweke & Williamson 1998*b*; Thompson *et al.* 2001). In addition, there are strong arguments that support the cooperative nature of the instability, such as the visualizations and feedback mechanism presented in Williamson (1996). In § 5.3.3, evidence of the elliptical nature of mode T3 was presented, and the cooperative mechanism of this instability was verified. The difference in the symmetry in relation

to mode A can be explained using kinematic arguments. The interaction between the two elliptical vortices happens predominantly in the cross-stream direction, whereas in the flow around a single cylinder this interaction happens in the streamwise direction. A different symmetry in mode A was also observed in the flow in a periodically driven cavity (Blackburn & Lopez 2003). The kinematic argument can be used in that case too; since the vortices are confined to the cavity and are not convected, their interaction takes place on a line perpendicular to the symmetry plane, and this is similar to what is observed for mode T3. In conclusion, the common characteristics of modes T3 and A indicate that these two modes are actually the same type of instability.

7. Conclusion

The secondary instabilities that occur in the early stages of the transition in the wake for the flow around two identical circular cylinders in tandem arrangements were investigated by means of linear stability analysis and three-dimensional direct numerical simulations. The results were compared to the isolated cylinder case, and the different scenarios observed depended fundamentally on the separation between the cylinders.

If the separation was less than the drag inversion spacing, the downstream cylinder had a stabilizing effect in the flow. For such cases, the three-dimensional structures appeared later in terms of Reynolds number than for the flow around an isolated cylinder. In addition, the topologies of the unstable modes for these configurations were different from those observed in the flow around a single cylinder. It was shown that for configurations at shedding regime *SG*, the unstable mode at the onset of the secondary instability originated at the formation region, downstream of the leeward cylinder. This mode, referred to as mode T1, has a topology that breaks the spatial symmetry of the base flow, and its physical mechanism appears to be associated to a hyperbolic instability, indicating that mode T1 may actually be a manifestation of the single cylinder mode B. For slightly larger separations, the shedding regime changed to *AG* and a different unstable mode, named mode T2, was observed. Mode T2 had its origin at the base of the downstream cylinder, upstream of the vortex formation region. A centrifugal instability in this region seems to give rise to this mode. Like the single cylinder mode A, mode T2 wake topology keeps the in-plane spatial symmetry observed in the base flow. If the separation is increased a little more, but not so much as to change the base flow shedding regime, a new unstable mode (mode T3) is initiated at the interstitial region. Like modes B and T1, mode T3 also breaks the spatial symmetry of the base flow. Some of the mode attributes suggest that the underlying physical mechanism is a cooperative elliptical instability, so mode T3 could be interpreted as a manifestation of the single cylinder mode A, despite the different symmetries of the two. This difference can be explained by the distinct kinematics in each of the base flows.

On the other hand, if the separation was greater than the drag inversion spacing (shedding regime *WG*), the initial stages of the transition in the wake occurred in a similar way to that of the isolated cylinder. The first instability, mode A, arose earlier in Reynolds number terms when compared to the single cylinder case, and it is therefore concluded that the downstream cylinder has a destabilizing effect on the flow for separations larger than the drag inversion spacing. Curiously, the downstream cylinder had the opposite effect on mode B instability, delaying its bifurcation, as predicted by linear stability analysis. However, these different behaviours are consistent with

previously proposed physical mechanisms for the origin and sustainment of these modes.

This comprehensive study shows the different ways in which the early stages of the transition scenario respond to flow interference. A full characterization of the secondary instabilities and an evaluation of the relationship between the early stages of the wake transition and the centre-to-centre distance between the cylinders is presented in this paper; these are fundamental contributions towards a better understanding of the effects of wake interference in the flow around bluff bodies. The level of complexity of the changes in the early stages of the wake transition should discourage any extrapolation from isolated body results to multiple body configurations. We believe that the results and conclusions presented here can be used as guides in the careful assessment of the flow interference effects that are necessary prior to scientific or engineering work on flows around multiple bodies.

Bruno S. Carmo thankfully acknowledges CAPES-Brazil for financial support during his PhD at Imperial College London and Hilary Glasman-Deal at ELSP-IC for advice regarding the use of English. Julio R. Meneghini wishes to acknowledge FAPESP, CNPq, Finep and Petrobras for financial support. Spencer J. Sherwin would like to acknowledge financial support under an EPSRC advanced research fellowship.

REFERENCES

Barkley, D., Gomes, M. G. M. & Henderson, R. D. 2002 Three-dimensional instability in flow over a backward-facing step. *J. Fluid Mech.* **473**, 167–190.

Barkley, D. & Henderson, R. D. 1996 Three-dimensional Floquet stability analysis of the wake of a circular cylinder. *J. Fluid Mech.* **322**, 215–241.

Bayly, B. J. 1986 Three-dimensional instability of elliptical flow. *Phys. Rev. Lett.* **57** (17), 2160–2163.

Bayly, B. J. 1988 Three-dimensional centrifugal-type instabilities in inviscid two-dimensional flows. *Phys. Fluids* **31** (1), 56–64.

Beaudoin, J. F., Cadot, O., Aider, J. L. & Wesfreid, J. E. 2004 Three-dimensional stationary flow over a backward-facing step. *Eur. J. Mech.* B-*Fluids* **23** (1), 147–155.

Biermann, D. & Herrnstein, W. H., Jr 1933 The interference between struts in various combinations. *Tech. Rep.* TR 468. NACA.

Billant, P., Brancher, P. & Chomaz, J. M. 1999 Three-dimensional stability of a vortex pair. *Phy. Fluids* **11** (8), 2069–2077.

Blackburn, H. M. & Lopez, J. M. 2003 The onset of three-dimensional standing and modulated travelling waves in a periodically driven cavity flow. *J. Fluid Mech.* **497**, 289–317.

Blackburn, H. M., Marques, F. & Lopez, J. M. 2005 Symmetry breaking of two-dimensional time-periodic wakes. *J. Fluid Mech.* **522**, 395–411.

Brede, M., Eckelmann, H. & Rockwell, D. 1996 On secondary vortices in the cylinder wake. *Phys. Fluids* **8**, 2117–2124.

Carmo, B. S. & Meneghini, J. R. 2006 Numerical investigation of the flow around two circular cylinders in tandem. *J. Fluids Struct.* **22**, 979–988.

Carmo, B. S., Sherwin, S. J., Bearman, P. & Willden, R. 2008 Wake transition in the flow around two circular cylinders in staggered arrangements. *J. Fluid Mech.* **597**, 1–29.

Deng, J., Ren, A. L., Zou, J. F. & Shao, X. M. 2006 Three-dimensional flow around two circular cylinders in tandem arrangement. *Fluid Dyn. Res.* **38**, 386–404.

Gerrard, J. H. 1966 The mechanics of the formation region of vortices behind bluff bodies. *J. Fluid Mech.* **25** (2), 401–443.

Henderson, R. D. 1997 Nonlinear dynamics and pattern formation in turbulent wake transition. *J. Fluid Mech.* **352**, 65–112.

Igarashi, T. 1981 Characteristics of the flow around two circular cylinders arranged in tandem. *Bull. JSME* **24** (188), 323–331.

Jeong, J. & Hussain, F. 1995 On the identification of a vortex. *J. Fluid Mech.* **285**, 69–94.

Karniadakis, G. E. 1990 Spectral element–Fourier methods for incompressible turbulent flows. *Comput. Methods Appl. Mech. Engg* **80**, 367–380.

Karniadakis, G. E., Israeli, M. & Orszag, S. A. 1991 High-order splitting methods for the incompressible Navier–Stokes equations. *J. Comput. Phy.* **97**, 414–443.

Karniadakis, G. E. & Sherwin, S. J. 2005 *Spectral/hp Element Methods for Computational Fluid Dynamics*, 2nd edn. Oxford University Press.

Lagnado, R. R., Phan-Thien, N. & Leal, L. G. 1984 The stability of two-dimensional linear flows. *Phys. Fluids* **27** (5), 1094–1101.

Lasheras, J. C. & Choi, H. 1988 Three-dimensional instability of a plane free shear-layer – an experimental study of the formation and evolution of streamwise vortices. *J. Fluid Mech.* **189**, 53–86.

Leweke, T. & Williamson, C. H. K. 1998*a* Cooperative elliptic instability of a vortex pair. *J. Fluid Mech.* **360**, 85–119.

Leweke, T. & Williamson, C. H. K. 1998*b* Three-dimensional instabilities in wake transition. *Eur. J. Mech.* B/*Fluids* **17** (4), 571–586.

Meneghini, J. R., Saltara, F., Siqueira, C. L. R. & Ferrari, J. A., Jr 2001 Numerical simulation of flow interference between two circular cylinders in tandem and side-by-side arrangements. *J. Fluids Struct.* **15**, 327–350.

Mittal, S., Kumar, V. & Raghuvanshi, A. 1997 Unsteady incompressible flows past two cylinders in tandem and staggered arrangements. *Intl J. Numer. Methods Fluids* **25**, 1315–1344.

Mizushima, J. & Suehiro, N. 2005 Instability and transition of flow past two tandem circular cylinders. *Phys. Fluids* **17** (10), 104107.

Oertel, H. (Ed.) 2004 *Prandtl's Essentials of Fluid Mechanics*, 2nd edn. Springer.

Papaioannou, G. V., Yue, D. K. P., Triantafyllou, M. S. & Karniadakis, G. E. 2006 Three-dimensionality effects in flow around two tandem cylinders. *J. Fluid Mech.* **558**, 387–413.

Pierrehumbert, R. T. 1986 Universal short-wave instability of two-dimensional eddies in an inviscid fluid. *Phys. Rev. Lett.* **57** (17), 2157–2159.

Provansal, M., Mathis, C. & Boyer, L. 1987 Bérnard-von Kármán instability: transient and forced regimes. *J. Fluid Mech.* **182**, 1–22.

Ryan, K., Thompson, M. C. & Hourigan, K. 2005 Three-dimensional transition in the wake of bluff elongated cylinders. *J. Fluid Mech.* **538**, 1–29.

Sheard, G. J., Thompson, M. C. & Hourigan, K. 2003 From spheres to circular cylinders: the stability and flow structures of bluff ring wakes. *J. Fluid Mech.* **492**, 147–180.

Sheard, G. J., Thompson, M. C. & Hourigan, K. 2004 From spheres to circular cylinders: non-axisymmetric transitions in the flow past rings. *J. Fluid Mech.* **506**, 45–78.

Slaouti, A. & Stansby, P. K. 1992 Flow around two circular cylinders by the random-vortex method. *J. Fluids Struct.* **6** (6), 641–670.

Tasaka, Y., Kon, S., Schouveiler, L. & Le Gal, P. 2006 Hysteretic mode exchange in the wake of two circular cylinders in tandem. *Phys. Fluids* **18** (8), 084104.

Taylor, G. I. 1923 Stability of a viscous liquid contained between two rotating cylinders. *Phil. Trans. R. Soc. Lond. Ser.* A **223**, 289–343.

Thomas, D. G. & Kraus, K. A. 1964 Interaction of vortex streets. *J. Appl. Phys.* **35** (12), 3458–3459.

Thompson, M. C., Leweke, T. & Williamson, C. H. K. 2001 The physical mechanism of transition in bluff body wakes. *J. Fluids Struct.* **15**, 607–616.

Tuckerman, L. S. & Barkley, D. 2000 Bifurcation analysis for timesteppers. In *Numerical methods for bifurcation problems and large-scale dynamical systems* (ed. E. Doedel & L. S. Tuckerman), IMA Volumes in Mathematics and its Applications, vol. 119, pp. 543–556. Springer.

Williamson, C. H. K. 1988 The existence of two stages in the transition to three-dimensionality of a cylinder wake. *Phys. Fluids* **31** (11), 3165–3168.

Williamson, C. H. K. 1996 Three-dimensional wake transition. *J. Fluid Mech.* **328**, 345–407.

Zdravkovich, M. M. 1972 Smoke observations of wakes of tandem cylinders at low Reynolds numbers. *Aeronaut. J.* **76**, 108–114.

Zdravkovich, M. M. 1977 Review of flow interference between two circular cylinders in various arrangements. *ASME J. Fluids Engng* **99**, 618–633.

Zdravkovich, M. M. 1987 The effects of interference between circular cylinders in crossflow. *J. Fluids Struct.* **1** (2), 239–261.